Joint NASA / DLR Aeronautics Design Challenge 2021

CHANGE

Cryogenic Hydrogen Aircraft No Greenhouse Emissions

Institute for Aeronautics and Astronautics
Department of Aircraft Design and Aerostructures
Prof. Dr.-Ing. A. Bardenhagen

Joint NASA / DLR Aeronautics Design Challenge 2021

CHANGE

Cryogenic Hydrogen Aircraft No Greenhouse Emissions

Team
Al Rashwany, Kotayba
Beck, Ramón
Feldhahn, Florian
Kracke, Lennart
Miertsch, Kristof
Nittka, Jan Frederik

Academic Support and Advisors
M.Sc. A. Gobbin
Prof. Dr.-Ing. A. Bardenhagen

Submitted on July 18st, 2021

Table of Contents

List of Figures

List of Tables

Nomenclature

Latin Symbols

Symbol	Unit / Definition	Designation
b	m	wing span
c	m	chord length
D	m	Diameter
E	N/m^2	Youngs modulus
g	m/s^2	Gravitational acceleration
I	m^4	Second moment of area
L	N	Lift
l	m	length
L/D	-	Lift-to-drag ratio
M	Nm	Moment
m	kg	Mass
q	Pa	Dynamic Pressure
S	m^2	Area
$\dot{Q}$	W	Heat flow
t	m	thickness
V	N	shear force
w	m	displacement
W	N	Weight
W/S	N/m²	Wing loading

Greek Symbols

Symbol	Unit	Designation
α	$W/m^2 K$	Heat Transfer Coefficient
η	-, -,$Pa \cdot s$	Dimensionless half span, Efficiency, dynamic Viscosity
ϵ	°	Wing tip twist
Λ	-	Aspect ratio
λ	-	Taper ratio

Indizes

Symbol	Designation
25	chord of 25 %
50	chord of 50 %
a	Airfoil
b	span
chem	Chemical
cmp	Compressor
COOP	Cultivation Of Oil Palms
COT	Crude Oil Transport
conv	Convective Heat Transfer
D	Drag
DD	Drag divergence
DISTR	Distribution
EOC	Extraction of CPO
f	Fuselage
FFUEL	Fossil Fuel COX-Crude Oil Extraction
fr	Friction
fc	Fuel cell
i	Induced
ins	Insulation
int	Intersection
K	Kelvin
L	Lift
LDS	Liquification Distribution Storage
m	Mean Chord
off	offset
PE	Power electronics
PROD	Production of Fuel
REF	Refining
s	Stabilizer vertical / horizontal
sh	strut force horizontal
sv	strut force vertical
seg	Mission Segment
hs	Horizontal stabilizer
TOC	Transport
tot	Total
tu	Turbulent
W	Wing
w	Downwash
wet	Wetted surface
z	z-direction

Gradient

<u>Abbreviations</u>

Abbreviation	Designation
AOA	Angle of Attack
CCW	Circulation Control Wing
CFK	Costs per Flown Kilometer
CROR	Counter-Rotating Open-Rotor
DOC	Direct Operating Costs
EIS	Entry Into Service
EU	European Union
FCA	Final Cruise Altitude
FST	Full Size Trolley
GHG	Green House Gas
HEX	Heat Exchanger
HLD	High Lift Device
HT	Horizontal Tail
JFK	John F. Kennedy Airport New York
KIAS	Knots Indicated Airspeed
LFL	Landing Field Length
LGF	Lift-Gain-Factor
LH2	Liquid Hydrogen
MLM	Maximum Landing Mass
MTOM	Maximum Take-Off Mass
MZFM	Maximum Zero Fuel Mass
NLF	Natural Laminar Flow
NOx	Nitrogen Oxides
OEM	Operating Empty Mass
PAX	Passengers
RF	Radiative Forcing
ROC	Rate of Climb
RPM	Revolutions per Minute
SAF	Sustainable Aviation Fuel
SBW	Strut-Braced Wing
SET	Specific Excess Thrust
SKC	Seat Kilometer Cost
SKO	Seat Kilometers Offered
TLAR	Top Level Aircraft Requirement
TOFL	Take-Off Field Length
TOM	Take-Off Mass
T/W	Thrust to Weight Ratio
VT	Vertical Tail

1 Introduction

1.1 A Need for Change

The aviation industry is at an important decision point. Recent natural disasters show, among other impacts, that human-made climate change has now become part of the everyday life of the population. This ensures that the issue of climate protection is having an ever greater influence on the formation of political opinion. With a total of 3% [1], aviation alone has a considerable influence on global carbon dioxide emissions. Although constant efficiency improvements are being achieved through technological developments, the growth of aviation due to increasing demand from emerging economies such as China and India puts this effect into perspective. Further problems arise from the emission of greenhouse gases at high altitudes, where they have much longer residence times [2]. Another challenge is the increasingly scarce oil reserves [3], which will inevitably lead to significant increases in the price of kerosene in the long term. The European Union (EU) has recognized these problems and, as part of Flightpath 2050, has issued a target to reduce CO2 emissions by 75% and NOx emissions by 90% [4]. For this reason, there is currently a major effort to use alternative fuels in aviation. Promising options include biofuels or battery electric aircraft. Biofuels have the problem that agricultural land must be used for production, which can also be used for food production. The battery-electric approach provides a large additional mass for higher ranges due to the energy density being too low, which, due to the snowball effect, makes the total weight of the aircraft so large that profitable operation is no longer possible. At present, therefore, great hopes are being placed in the use of hydrogen. The advantage of hydrogen is that it can be produced by electrolysis from renewable energy sources, enabling climate-neutral flight operations. Due to its high gravimetric energy density, 2.8 times less fuel mass is required. At the same time, four times more tank volume is required due to its lower volumetric energy density. To overcome these challenges, new aircraft configurations are needed. Therefore, in this work the project CHANGE will be presented as a promising solution.

1.2 Looking At Future Markets

The development of an aircraft starts with researches for possible customers and their markets. CHANGE has a required design range of 2,000 km and a passenger capacity of 150 passengers (PAX). These top level design requirements (TLAR) characterize it as a regional to short haul aircraft.

Every 15 years the amount of the worlds annual traffic has doubled in the last 50 years. Regardless of the current situation with COVID-19, it is to be expected that the annual traffic will double from 2018 to 2033 as well. This is assumed since the global population is expected to grow as well as the socio-economic middle class. Thereby, the financial ability to fly grows accordingly.

In 2018 the most added short-haul routes have been focused around the domestic market within China, the regional market within Europe and the domestic market inside the US. Additionally the domestic market inside India is expected to grow by 480 % in the next 20 years. As these are the identified most growing markets, CHANGE is fitting within this segment appropriately. The following graphics show this ability on great circle maps. The regions shown within are the most dense populated areas world wide and thereby the most relevant growing markets.[5] Airbus estimates 3,000 units to be sold in the short-haul market segment until 2038 beyond that even more can be expected.[6] Appendix B

As the public and political awareness of climate change grows, the restrictions for short haul flights with conventional fuels will increase as well. The EU has already begun to tax Greenhouse Gases (GHG). This trend will continue and impact the aviation industry in the near future. To counteract these developments, a change in aviation is necessary. A change which can begin with liquid hydrogen (LH2) as propellant. Today's LH2 price is relatively high in comparison to fossil fuels and sustainable aviation fuels (SAF). But this is not a situation necessary to last. As soon as the usage of LH2 progresses, the prices will drop and enable its economical usage in aviation. LH2 can be produced everywhere and is not bound to specific extraction sites. Through technological progress

of production, the amount and efficiency will increase and provide a GHG neutral fuel for aviation. This fact is additionally able to be used as marketing strategy to attract eco-conscious customers. CHANGE is meant to combine all these factors and use them for a brighter future.

2 Concept Of Design

This chapter details the main points in the design process of the aircraft. The first step in selecting the most promising configuration is the identification of TLAR from the competition assignment. An overview of the main parameters is given in Table 2.1. Mission 1 is to be optimzed for minimal climate impact and Mission 2 for both minimal climate impact and maximum economic efficiency.

Table 2.1: Selection of the Top-Level Aircraft Requirements for the Design Challenge 2021

Category	Description	Value
Payload	Passengers	150
	Payload mass	15,750 kg
Range	Range	>=2,000 km
	Diversion range	200 NM
Performance	Minimum operating height	3,000 m
	Cruise Speed	0,7 Ma
	Approach Speed	<=130 kts
Market	Entry into service	2035
	Fuel	Hydrogen
Design Missions	Mission 1	600 km
	Mission 2	2,000 km

Due to the nature of working in a multifaceted team with different fields of expertise, the first design camp had every member of team enter all their proposed concepts for the challenge. These concepts were discussed in detail and the most promising configurations were selected. The department heads investigated the relevant physical effects for these concepts and presented their conclusions and concerns in the second design camp. Because a quantitative examination of the different concepts is hardly possible at this early design stage, a qualitative study using a Harris matrix was conducted. The results are shown in Table 2.2.

Table 2.2: Harris matrix for the qualitative selection of the identified design concepts

	Emissions	Fuel efficiency	Noise reduction	Maintain-ability	Turnaround effiency	Passenger comfort	
	35%	25%	10%	10%	10%	10%	100%
BWB Fuel cell	2	2	2	-2	-2	-1	**0,9**
BWB Turboprop	1	1	1	-2	-2	-2	**0,1**
Box-Wing Fuel cell	2	1	1	1	-1	2	**1,25**
Box-Wing Turboprop	1	0	0	1	-1	1	**0,45**
SBW Fuel cell	2	2	1	2	2	2	**1,9**
SBW Turboprop	1	1	0	2	2	1	**1,1**

From this evaluation, the strut-braced wing (SBW) with a fuel cell powerplant was selected. This configuration completely eliminates nitrogen oxide (NOx) emissions. The only remaining GHG is

the water vapor generated by the fuel cell, which can build contrails. According to [7], below $8,000\,\text{m}$ the climate impact of water emissions in the atmosphere is negligible. Therefore, a cruise altitude of $8,000\,\text{m}$ was chosen as an additional TLAR. A preliminary design study of lower cruise altitudes showed severe impact on the fuel efficiency. The following sections discuss the key configuration characteristics and their influence on the overall concept.

2.1 Strut-Braced Wing

The SBW configuration, as one of the main design features of the proposed concept, provides many opportunities to improve fuel economy. The additional support of the wing structure allows to increase the aspect ratio of the wing, which achieves a reduction in lift induced drag. Another possibility is the use of thinner airfoils, which in turn decreases the wave drag of the wing and therefore reduces the required sweep angle. This in turn enables the application of Natural Laminar Flow (NLF) airfoils to lessen the vicious drag of the wing. These factors must be balanced against an increase in viscous drag by the strut and the interference drag caused by the interfaces between wing and strut [8]. Furthermore, the reduced space in the airfoil is of no concern for a hydrogen-based aircraft, because placing the tank in the wing is unfeasible.

2.2 High-Lift Devices

Conventional high-lift systems require more element fowler flaps to achieve high lift coefficients, which come with high structural masses, and disturbances of the airfoil geometry. Furthermore, they are responsible for substantial noise development during Take-Off and Landing. Circulation control represents an alternative that partially eliminates the problems of conventional high-lift systems.

The Circulation Control Wing (CCW) consists of a simple plain flap, with 25 percent of chord length, which is blown out internally in order to delay the trailing edge separation by additional energy input into the boundary layer. In this way, high angles of attack and lift coefficients can be achieved in combination with suitable leading edge systems.[9]
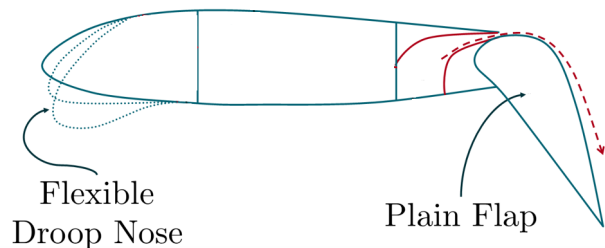
Figure 2.1: Circulation Control Wing

Because of the simple geometry, it has the potential to reduce the control surface weight, while achieving even higher lift coefficients. This is partially compensated, by additional weight due to compressors, power generation and related systems, like pneumatic lines. Since the climb phase represents the highest power demand, there is enough excess power available during takeoff and landing to operate the CCW. With highly efficient axial compressors, the additional mass is kept within limits.

Slotted leading edge devices are discarded because the discontinuity in the wing contour forces a boundary layer transition, negating the advantages of natural laminar flow. The Droop nose is an unslotted leading edge device capable of generating higher angles of attack by rotating the leading edge downward while preventing surface edges. However, the rigidness of the conventional droop nose creates a discontinuity in the camber and surface of the airfoil, this leads to high pressure peaks at the transition, forcing an early separation, which results in low achievable maximum angles of attack in combination with CCW [10]. The flexible droop nose changes the contour of the leading edge in such a way that a continuous camber line is created and there is no discontinuity on the wing surface. This smoothes the pressure distribution and prevents leading edge separation[11] [12]. Figure 2.1 shows a principle sketch of the CHANGE high lift system.

2.3 Powerplant

Using hydrogen as a fuel enables the incorporation of new technologies besides gas tubines which have been fitted for hydorgen combustion. In addition, various hybrid concepts of the two technologies are feasible . A brief overview of possible combination and their overall efficiency is given in Appendix Appendix C.

Conventional turbo engines are a valid choice as a powertrain and propulsion system. Firstly integration and handling of turbo engines in airplanes are widely studied. Secondly burning hydrogen in turbo engines is generally possible and their efficiency can be improved while pollutant emissions decreased [13]. However, combustion engines are still less efficient than a fuel cell powerplant. This becomes even more important with regard to high fuel costs of hydrogen. Even though a hydrogen fueled jet engine emits fewer pollutants, they are not free of them. Fuel cells in contrary only emit water vapour and when limiting the cruise altitude to $8000\,\mathrm{m}$ the impact of contrails on earths atmospheric temperature is negligible [14]. With this in mind the decision is made to base the powertrain on fuel cells. A power density of $5.5\,\mathrm{kW/kg}$ on stack level is assumed with an addition of $3\ ^{kg_{aux}}/_{kg_{fc}}$ for auxilliaries [15]. According to CS-E, jet engines are required to accelerate from a 15% to a 95% power or thrust setting within 5 seconds. Ramp up times of around $1\,\mathrm{s}$ omit the necessity of large and heavy buffers, like Li-Ion batteries or super capacitors for peaks in power demand[16]. Concerning the use of fuel cells, thermal management is a key challenge to overcome. While operating at higher efficiency rates at over 60% compared to internal combustion engines and therefore generating less heat in total [17], they discharge only about 3% of the generated heat over the exhaust [18]. While some of the heat can be used to heat up the hydrogen, they still generate a substantial amount of heat that needs to be dissipated, thus a heat exchanger (HEX) is required [19].
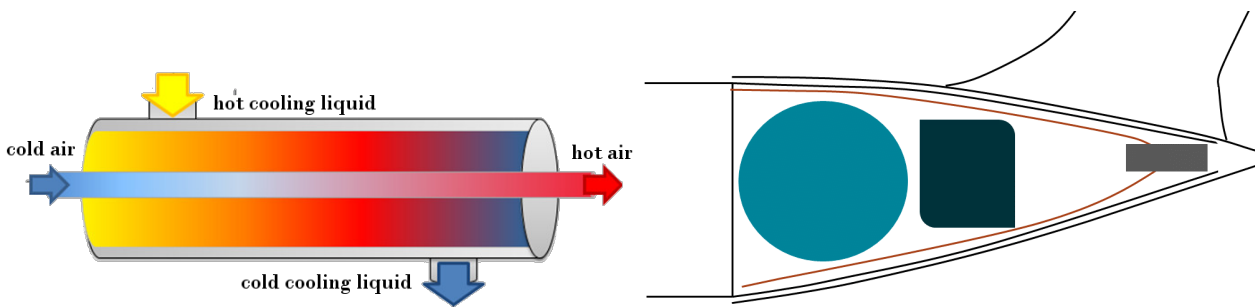
Figure 2.2: Sketch of one double-walled HEX pipe [20] **Figure 2.3**: Sketch of HEX tailcone integration (not to scale)

The HEX consists of multiple double-walled pipes mounted around the outer circumference of the rear end section, as illustrated in Figure 2.2. Cold ambient air passes through the pipe and heating up, while the warmer coolant circulates on the inside of the double walled pipe and cooling down. The draft in Figure 2.3, which is only a schematic sketch and not to scale, shows a cross section of the rear end of the aircraft. For orientation, the tank, fuel cell and compressor of the CCW system are indicated qualitatively. The double walled section houses the pipes for the HEX and also functioning as boundary layer ingestion system in interaction with the CCW system. During Take-Off and Landing the ambient air is sucked into the HEX pipes, described in 2.2, by the compressor of the CCW system. Therefore ingesting the boundary layer of the fuselage. After passing the compressor the air is then directed through pneumatic ducts to the wing. For Climb, Cruise and Descend the CCW system is deactivated. During these segments the air exits the pipes at the end of the tailcone section.

2.4 Counter-Rotating Open-Rotor

As the cruise Mach number is limited to $Ma_{cruise} = 0.7$ both turbo prop and turbo jet engines operate at a similar propulsive efficiency therefore it is feasible using a propeller to generate thrust [21]. Since the thrust requirements for an aircraft in this weight class are likely to exceed the

performance capabilites of two propellers, four propellers are chosen in a Counter-Rotating Open-Rotor configuration (CROR) to benefit from the increase in efficiency that this arrangement entails [22]. Based on the choice of using a fuel cell powertrain, electric engines are used to drive the propellers. Demonstrated in Figure 2.4 and illustrated by the bold black lines, each electric engine is connected to one of the two propellers per unit via a drive shaft and isolated from each other by a flame protection wall, bold red lines.
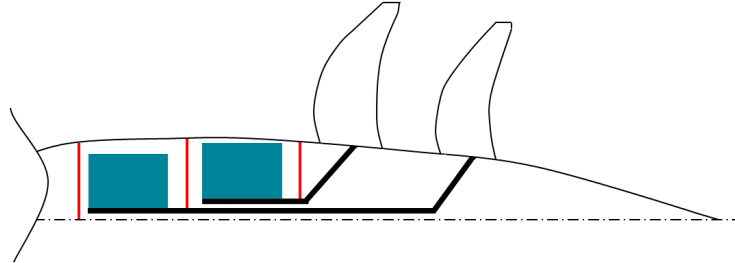
Figure 2.4: Sketch of propulsion unit (not to scale)

This makes it feasible to view this engine propeller combination inside one CROR unit independed from the other. Making it a four engine aircraft integrated into two propulsion units. Thus reducing the necessary excess thrust for the one engine off failure case at Take-Off.
Two Counter-Rotating Open Rotor units are mounted behind the wing in a pusher configuration. This is due to the characteristics of the laminar flow wing described earlier.

2.5 Hydrogen Tank

The high gravimetric energy density of hydrogen is a major advantage over other propellants. In comparison to Kerosene or sustainable aviation fuel it has a 2.8 times bigger gravimetric energy density. This holds the potential of substantial weight savings. However, the low volumetric energy density is a challenge. It is necessary to store the hydrogen either under high pressure or as a liquid at cryogenic temperatures below -252.8°C at atmospheric pressures. High pressure storage minimizes the weight saving aspect by far, making it not suitable for larger aircrafts. High pressure storage has a gravimetric density of around 6.5% [23], while liquid hydrogen storages can reach up to 70% [24]. Hydrogen has a volumetric energy density 4 times higher than kerosene, resulting in a larger tank volume.
The location of the hydrogen tank is chosen in the rear aft section of the fuselage behind the pressure bulk of the cabin (see Figure 2.3). The fuel system consists of pumps and insulated lines from the tank to the fuel cell and pumps.

2.5.1 Structure

The structural mass of the tank system depends on the maximum allowable pressure, which is set to 1.5 bar. Because of the extensive experience with aluminum as a structural material for hydrogen tanks and the low structural load, aluminum is chosen as material.

2.5.2 Insulation and heat management

The low temperature of liquid hydrogen requires an insulation to minimize heat flow, which causes vaporization and therefore increasing pressure. Excess heatflow causing a rise of pressure above the designed pressure and requires venting. Contrary, the tank pressure may not fall below atmospheric pressure to avoid leakage of air into the tank, thus a certain vaporization is needed during high power demand. To ensure the mass flow in high power phases, heat must be supplied, thus a heating system is required, the fuel cell excess heat is used partially for this task. The insulation consists of a low density foam. Its thickness is designed to ensure a sufficient holding time without the need of excessive venting.
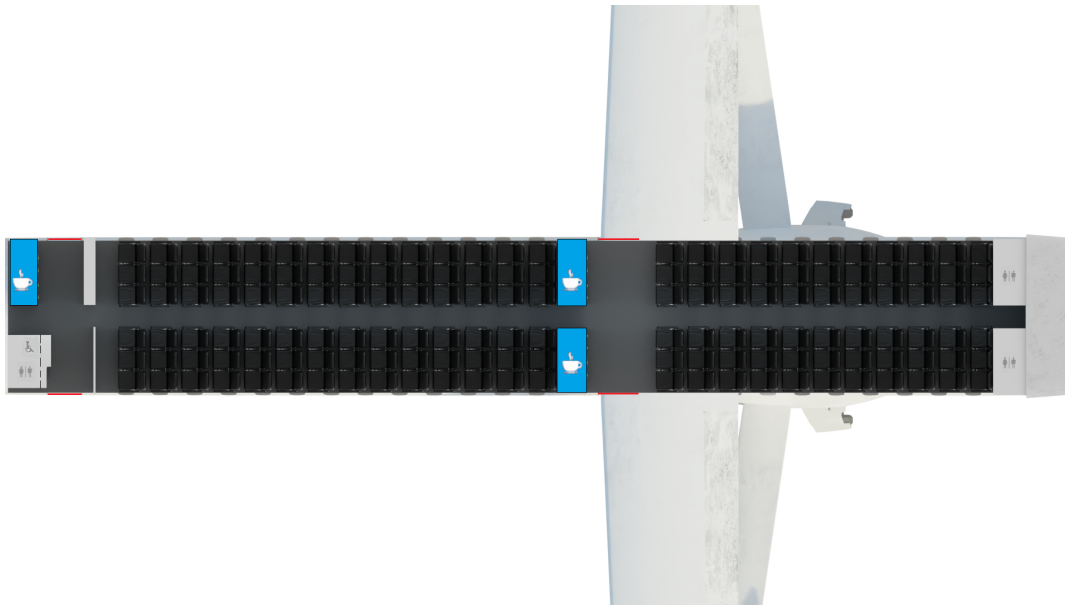
Figure 2.5: Cabin Layout

2.6 Cabin

The general fuselage concept describes a standard narrow-body design with an outer diameter of 3.8 m and a cabin diameter of 3.7 m. The overall length is 38.1 m, divided in cockpit section with a length of 2.99 m , constant section 24.91 m and tail cone with a length of 10.2 m. The reason for choosing a standard narrow-body design is mainly the existing airport infrastructure which is construed for today's aircraft layouts. The main part of the constant section is filled out by the cabin. It has been designed as reference to dimension the fuselage. To provide an adequate usability all CS-25 regulations have been considered. The designed passenger cabin as seen in Figure 2.5. has to emergency exits on each side. The front emergency exit has the size of a Type B exit but is certificated as Type C exit to reduce the necessary space used for the cross aisles. Located in the front cross aisles, are a galley with four full size trolley (FSTs), the cockpit door, a lavatory which fits the requirements to be used by persons with reduced mobility and a storage compartment. Additionally the front lavatory is equipped with an extension mechanism. This enables it to require only the space for a standard lavatory but extend a wall to fit an assistance person for persons with reduced mobility if necessary. At the chosen location, the extension does use space, not required in flight. From there on fourteen passenger seat rows à six seats begin and lead to a five FST galley on each side in front of a Type A emergency exit. This exit type has been chosen to fulfill evacuation requirements and provide a larger opening to access the galley easier. Behind the exit's cross aisle eleven seating rows follow. The cabin ends with two standard lavatories. This configuration efficiently reduces the necessary length of the cabin while providing an undisturbed workplace for the crew.

The space provided by the galleys and the storage compartment is sufficient to fit the role of a short-haul aircraft. Seating distance is 30 inch, so that a reconfiguration to fit more passengers or equip a two-class layout is possible.

All evacuation requirements are fulfilled with a total passenger flow of $165 PAX/90 s$ and 150 planned seats, three flight attendants according to the number of passengers and the required number of attendants per door. To fit the baggage of the passengers, overhead compartments and a bulk exist. The bulk area is small and only designed to fit baggage, no additional freight. Thereby the fuselage diameter can be reduced to reduce drag as well. The aft section of the airframe houses the tank and fuel cells. To fit the tank the constant section of the fuselage had to be lengthened durign according to the iterational calculated dimensions of tank and fuel cells.

3 Simulation Workflow

This chapter provides an overview of the simulation workflow in MATLAB and the associated functions used to calculate the aircraft characteristics. An overview of the simulation workflow is shown in Figure 3.6.
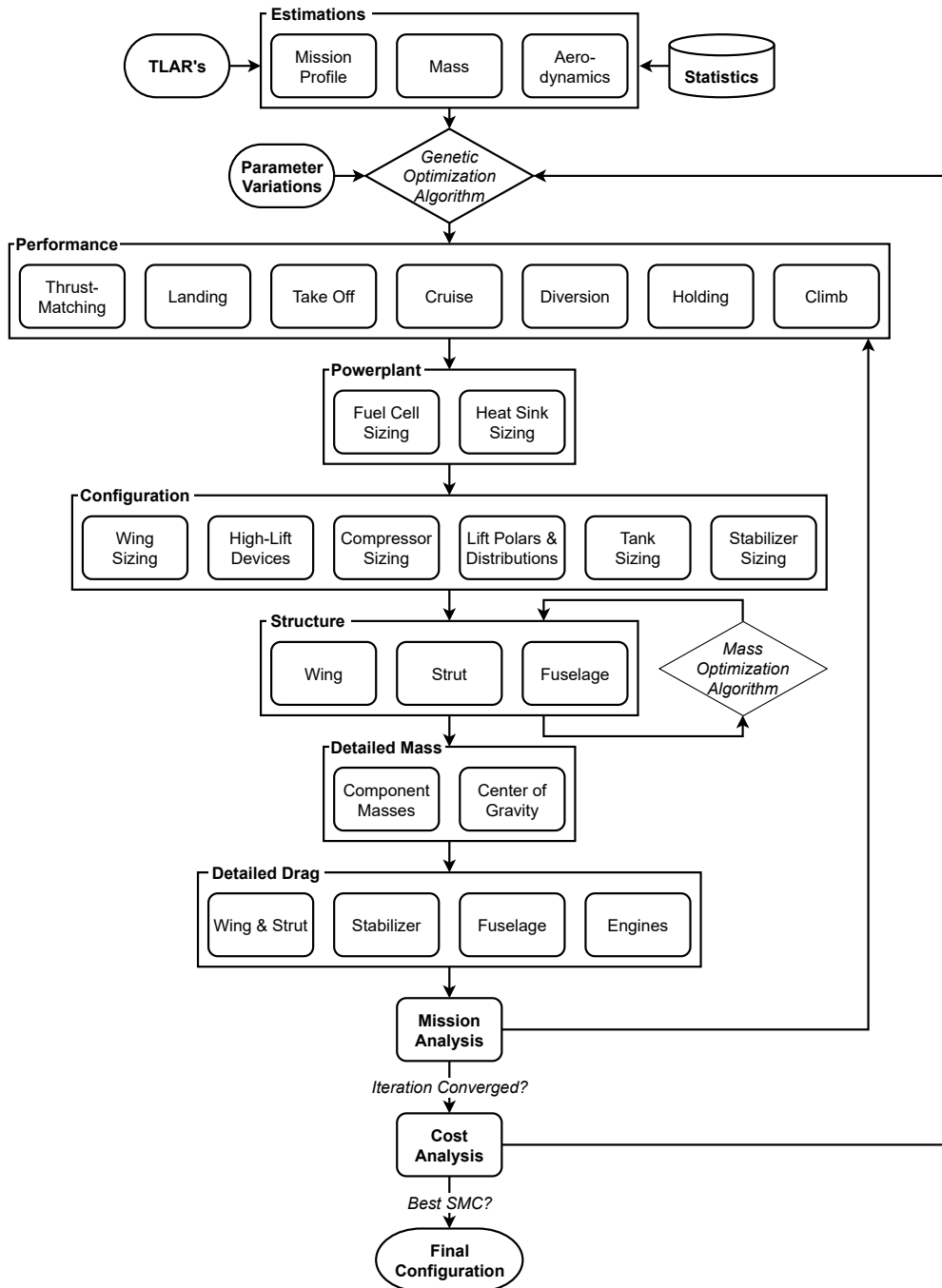
Figure 3.6: MATLAB Simulation Workflow Overview

The simulation workflow starts with a preliminary estimation of key aircraft parameters to set a starting point for the following optimization and iteration loop. The genetic optimization algorithm provided by the Global Optimization Toolbox of MATLAB takes these values and combines them with the parameter variations shown in Table 3.3. The goal of the optimization is to find the aircraft parameters for the lowest Seat Mile Cost (SMC). The simulation is run until the iteration loop converges to stable values. A cost analysis as described in section 3.10 is conducted on the results. The calculated SMC is then fed back to the optimization algorithm.

Table 3.3: Parameter variations and their upper and lower limits used for the Genetic Algorithm

Category	Parameter	Boundaries
Configuration	Aspect Ratio [-]	10-20
SBW	Strut force [N]	0 - $\frac{MTOM}{2}gG_{max}$
	Relative strut position [-]	0.1 - 1
	Strut offset [m]	0.1 - $\frac{c_{Wing,max}}{2}$

3.1 Estimations

To enable a shorter iteration process, reasonable initial values must be set before starting. As reference value for the CHANGE, the operating empty mass (OEM) is most important of these values. As existing reference for CHANGE the Airbus A220-300 has been chosen because of it's similarity in payload design. Thereby the OEM of the A220 has been used as a reference point. Because CHANGE is a non-existing aircraft concept with pre-market technology, an additional mass of 10t has been assumed as technology penalty. The further estimations needed to determine the weight of the tank and the weight of the fuel cells. Therefore, the overall required physical energy has been estimated with simplified flight mechanical calculations for climb, cruise, diversion and holding. Taxi, take-off and descend have been assumed as not fuel consuming. The aerodynamic efficiency of the aircraft was estimated as $\frac{C_L}{C_D} = 26$ because of the natural laminar flow wing. The fuel cell is sized by the highest required power during the flight and it's power density (assumed as $1.5^{MJ}/m^3$). The simplified efficiency of the fuel cell has been assumed as 50% to approximate the necessary amount of LH2 which again determines the size and weight of the tank. These first estimations provided enough input to start into the iteration process.

3.2 Performance

In the following the performance of the the conceptional aircraft, described in section 2., is assessed. This is done for each flight segment from Take-Off, through Climb and Cruise to Landing at the destination. In addition to the mission stretching 2,000 km an additional mission covering 600 km is studied with fixed TLAR's from the 2,000 km mission. Generally the Take-Off and Cruise segment determines the first dimensioning of performance parameters. More specific the Thrust to Weight ratio (T/W) for Take-Off and Cruise, which in turn is affected by the Take-Off Field Length (TOFL) and cruise altitude. However, the landing segment can become limiting for airplanes using LH2 as fuel. This is due to a higher gravimetric energy density of LH2, which leads to lower trip fuel mass and therefore a higher landing mass when compared to a convential aircraft using kerosine as its fuel. In combination with the maximum approach speed of 130 ktsthis leads to low overall wing loading and/or a higher lift coefficient.

3.2.1 Wing loading

To determine the Take-Off wing loading, the T/W ratio is formulated for Take-Off, Climb and Cruise, which can be obtained from equations of motion. Those ratios are plotted in Figure 3.4. over various wing loading values. This diagram is then used to chose the optimum wing loading for a minimal T/W ratio.

3.2.2 Take-Off

As mentioned above the TOFL is the decisive factor which influences any other Take-Off performance parameter. In fig. 3.4 a simplified version of T/W_{TO} is shown. The performance characterisics of the aircraft for Take-Off were determined to meet the requirements for an one engine inoperable event.

3.2.3 Climb

It is generally desired to climb as fast as possible, therefore a high Rate of Climb (ROC) is beneficial. Firstly to exceed $10,000$ ft ft in order to escape the 250 KIAS speed limitation and secondly to maximize the time at optimum performance in cruise. The ROC can be derived from the Specific
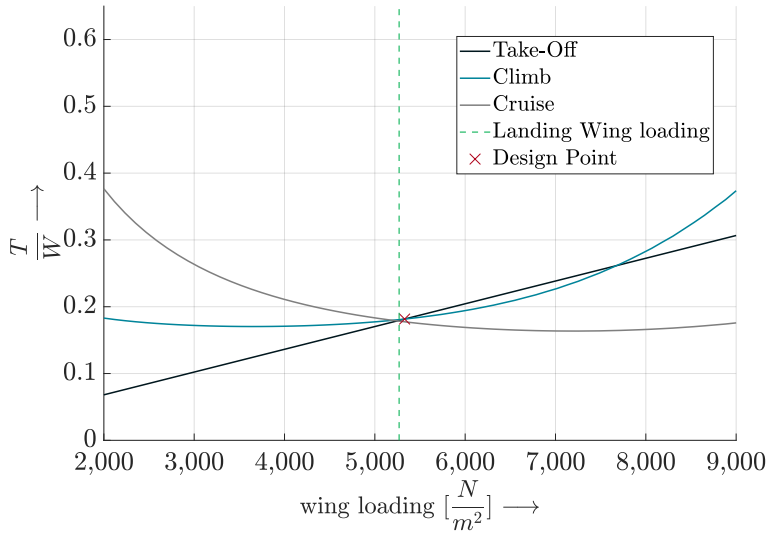
Figure 3.7: Wing loading matching

Table 3.4: Performance parameters for wing loading matching

Parameter	Value
TOFL	$2,000\,\mathrm{m}$
T_{TO}	$152\,\mathrm{kN}$
$(T/W_{TO})_{TO}$	0.22
$(W/S)_{TO}$	$5,371\,\mathrm{N/m^2}$
$C_{L,TO}$	1.9
ROC	$11.5\,\mathrm{m/s}$
V_{CL}	$425\,\mathrm{km/h}$
Ma_{CR}	0.7
$(C_L/C_D)_{TO}$	9
$(C_L/C_D)_{CL}$	24.6
$(C_L/C_D)_{CR}$	25.7

Excess Thrust (SET). Equation (3.1) defines the SET γ_E for a stationary climb.

$$\gamma_E = \frac{T - D}{W} \qquad \mathrm{D} = C_D \cdot q \cdot S \qquad (3.1)$$

The drag coefficient used to calculate SET derives from the drag polar specific to this aircraft. While thrust T is the maximum available thrust derived from the thrust model in described in section 3.3. A mean optimum ROC is obtained from examining optimum climb rates for various airspeeds. This mean optimum ROC equals 11.45 m/s. Other climb rates for an array of airspeeds are shown in Figure 3.8.
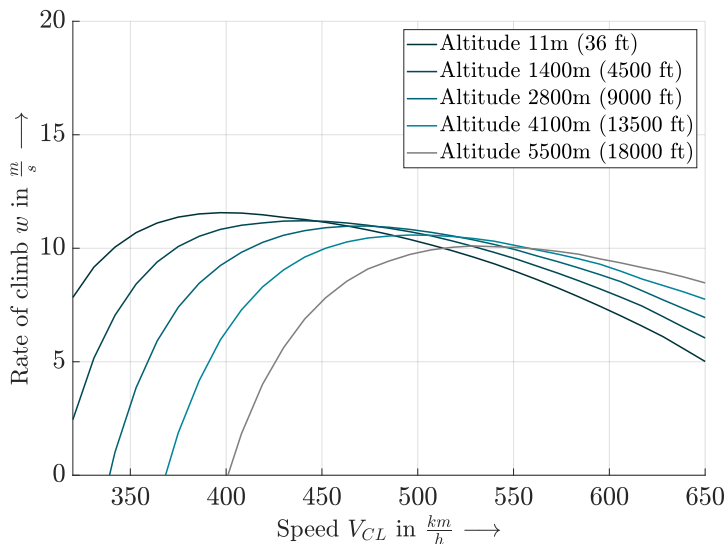
Figure 3.8: Rate Of Climb

Table 3.5: Performance parameters climb

Parameter	Value
w_{CL}	$11.5\,\mathrm{m/s}$
V_{CL}	$425\,\mathrm{km/h}$
P_{CL}	$15.2\,\mathrm{MW}$

$$C_L = \frac{W}{S \cdot q} \qquad (3.2)$$

3.2.4 Cruise

Two of the main cruise performance parameters have limitations. The Cruise Mach number is fixed at 0.7 and the Final Cruise Altitude (FCA) has an upper limit at $8,000\,\mathrm{m}$ due to the negligible effect of contrails on the radiative forcing (RF) below this altitude [25]. To determine the necessary

Table 3.6: Performance parameters cruise

Parameter	Value
V_{CR} (Ma_{CR})	776 km/h (0.7)
T_{CR}	27.72 kN
$C_{L,CR}$	0.44
$C_{D,CR}$	0.0171
$(C_L/C_D)_{CR}$	25.7
ICA	7,925 m
FCA	8,000 m

Table 3.7: Performance parameters landing

Parameter	Value
V_{app}	125 kt/s
$C_{L,LDG}$	3.55
$C_{L,CR}$	0.44
$(C_L/C_D)_{LDG}$	6
LFL	780 m

thrust at cruise to maintain speed and altitude, the L/D ratio for this segment needs to be calculated. The lift coefficient is obtained from Equation (3.2). The drag coefficient is obtained by studying the drag of different aircraft components in more detail as discussed in Section 3.8.

3.2.5 Landing

As described in Section 3.2 the lower burnt fuel mass equals in a lower landing wing loading when compared to a conventional aircraft. Therefore, a high lift coefficient is necessary to stay below 130 kts approach speed and keeping the wing loading at a moderate level. With a landing wing loading of $5,336$ N/m² this results in a landing lift coefficient $C_{L,LDG} = 3.55$ with at an approach speed of 125 kts. This is, as expected, the highest necessary lift coefficient and therefore determines the high-lift devices(HLD). Thus, making a CCW system necessary.

3.3 Propulsion

The two propulsion units each contain two identical, but counter rotating, electric engines each connected to a propeller via a shaft.

3.3.1 Electric engine

As stated in Section 3.2, the maximum power required stems from the climb segment with $P_{max} = 15.2$ MW. In total there are four electric engines requiring each engine to provide 3.8 MW. A suitable electric engine for this aircraft is the Siemens SP2000 [26]. As one SP2000 delivers around 2 MW two electric engines could be coupled together to reach the required Power of 3.8 MW. Since there is little to no available data for this and other electric engines in this power class, performance characteristics of an EMRAX 348 have been scaled to match the power necessary for this application [27]. As detailed performance characteristics like Torque over Revolutions Per Minute (RPM) and Power over RPM are needed to be able to size the propeller and calculate available thrust in each mission segment. Power electronincs have been approximated with 40kW/kg [28].

3.3.2 Propeller

To approximate the optimum propeller diameter for the given engine power The Generalized Method of Propeller Performance Estimation from Hamilton Standard was applied. Performance maps for the NASA SR-3 are used to determine the propeller performance for varying operating conditions[29]. The main objective is on finding the optimum propeller diameter for a given cruise thrust, Mach number, altitude and RPM, where the necessary engine power is minimal. As shown in Figure 3.9. a slightly larger diameter would be beneficial in power consumption but a larger diameter would exceed the Blade tip limitation. Therefore the propeller diameter is kept at 3.74 m.

3.4 Powerplant

Sizing the powerplant is divided into two parts, fuel cell and thermal management system. Sizing the fuel cell itself is based on the power demand of the aircraft. While the thermal management system is determined by the efficiency at which the fuel cell operates at any given mission segment.
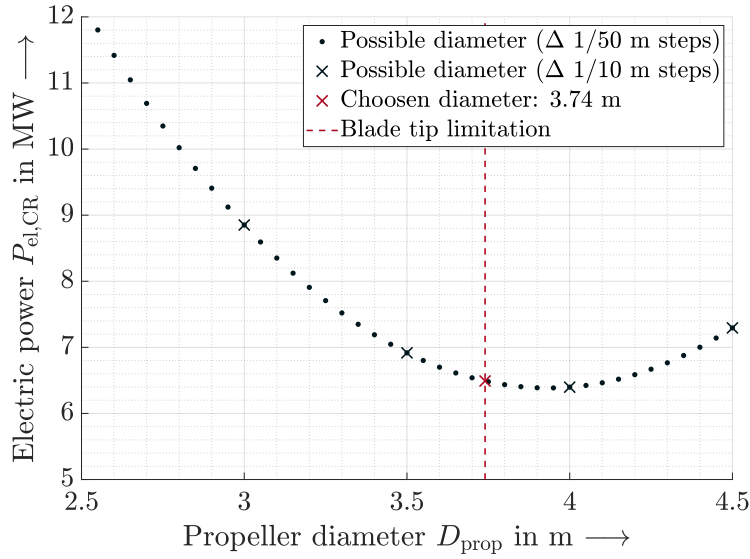
Figure 3.9: Propeller diameter sizing

Table 3.8: Parameters electric engine [28]

Parameter	Value
RPM	$1{,}620 \, ^1/_{\text{min}}$
P	$3.8 \, \text{MW}$
$^P/_m$	$7.66 \, ^{\text{kW}}/_{\text{kg}}$
$^P/_{m_{PE}}$	$40 \, ^{\text{kW}}/_{\text{kg}}$

3.4.1 Fuel cell

The sum of power demands of all components determines the necessary power that the fuel cell is required to provide. Table 3.9. lists the biggest power consumers, where $P_{aircraft}$ is the power demand of an more electric aircraft. This incorporates the power for avionics, actuators, cabin ventilation and entertainment. The power required was estimated on the basis of the power provided by the Trent 1000 [30]. With addition of the CCW system, this totals in 17.1 MW.

Table 3.9: Power demand components

Parameter	Value
$P_{aircraft}$	$0.5 \, \text{MW}$
P_{CCW}	$1.4 \, \text{MW}$
P_{CL}	$15.2 \, \text{MW}$
P_{total}	$17.1 \, \text{MW}$

Therefore with a power density of $5.5 \, ^{\text{kW}}/_{\text{kg}}$ the overall stack weight is 3,110 kg and 9,330 kg for auxilliaries. Auxilliaries contain all systems, like mounting brackets, plumbing, HEX, pumps, cables and stack management system, to operate a fuel cell [15]. This results in the total weight of the powerplant of 12,440 kg.

3.4.2 Thermal management

As described in Section 2.3. heat management is one of the key challenges when using fuel cells in aviation. To determine the heat generated by the fuel cell, a generic performance chart which maps the efficiency of the fuel cell over the corresponding power level is used[31]. Additionally the heat flow generated is subtracted by 3%, this is due to heat heat dissipated over the hot exhaust water vapour [18]. With this efficiency the heat generated can be calculated using the Equation (3.3). [32].

$$\dot{Q} = (1 - \eta_{fc}) \cdot P_{tot,seg} \tag{3.3}$$

To reduce the amount of heat the HEX has to dissipate, some of it can be used to heat up the hydrogen before it enters the fuel cell, with $T_{inlet,fc} = 302.15 \, \text{K}$ and $T_{LH2} = 33 \, \text{K}$ [19]. The reduction of heat flow by heating up hydrogen can be calculated by Equation (3.4). With $c_{P,H2} = 14.31 \, ^{\text{kJ}}/_{\text{kgK}}$

[33].

$$\dot{Q}_{fuel} = \dot{m}_{fuel} \cdot c_{P,H2} \cdot \Delta T_K \tag{3.4}$$

$$\Delta T_K = T_{inlet,fc} - T_{LH2}$$

The convective heat flow can be calculated with Equation (3.5). The heat transfer coefficient (htc) can be obtained via a Nusselt correlation for turbulent flow in a circular tube see Equation (3.6) - (3.7) [32].

Table 3.10: HEX parameters

Parameter	Value
Number of Pipes	560
l_{pipe}	$10.2\,\mathrm{m}$
D_{pipe}	$2\,\mathrm{cm}$
$m_{tot,HEX}$	$440\,\mathrm{kg}$

$$\dot{Q}_{conv} = \alpha \cdot S_{pipe} \cdot \Delta T_K \tag{3.5}$$

$$Nu = 0.023 Re^{0.8} \cdot Pr^{0.4} \tag{3.6}$$

$$\alpha = \frac{Nu \cdot \lambda}{l_{pipe}} \tag{3.7}$$

$$Re = \frac{\rho \cdot v \cdot D_{pipe}}{\eta}.$$

$$Pr = 0.7$$

With the parameters in Table 3.10. and Equations (3.5) - (3.7) the Number of Pipes at their weight can be estimated.

3.5 Configuration

The purpose of this section of the iteration loop is the definition of the relevant parameters of the aircraft surfaces and the dimensioning of the hydrogen tank.

3.5.1 Wing Aerodynamics

The first step of the analysis of the wing aerodynamics is the definition of the wing geometry. The planform is derived from the calculated MTOM and the wing loading as described in section 3.2. Further geometric constraints such as aspect and taper ratio are set by the optimization algorithm within the defined boundaries. The resulting values are shown in Table 4.15. The next step is the selection of the correct airfoil to archieve a NLF condition. Because the design of an optimal airfoil is beyond the scope of the work, a literature search of existing airfoils that fit the mission requirements was conducted. The selected airfoil is the S207 from [34]. This slotted airfoil is optimized for NLF at a Mach number of 0.7, which is the exact Mach number required by the TLARs. At this speed and the cruise lift coefficient calculated in Section 3.2. it achieves a L/D of 150. At lower speeds of Ma = 0.2 the airfoil provides a high c_L of 2.23, which greatly alleviates the need for a elaborate system raising the Take-Off and Landing lift coefficients.

The analysis of the lift distribution and polars is based on the work by Diederich [35]. The method is modified to account for the effects of the high-lift devices described in the following section by adding another circulation factor γ_c to Equation (3.8).

$$\gamma = \underbrace{\gamma_a \cdot C_{L,W} + \gamma_b}_{\text{Original Diederich}} + \gamma_c \tag{3.8}$$

Modified Diederich

γ_c is determined in the same way as the circulation factor resulting from wing twist γ_b by adding an equivalent Angle of Attack (AoA) in the wing section where HLD are used, The AoA is calculated using the airfoil lift gradient and the additional lift coefficient generated by the HLD. From these results, the lift distributions at the different flap configurations of the aircraft are calculated.

3.5.2 High Lift Devices

The high lift device consist of leading edge flexible droop nose and trailing edge internally blown flap. Trailing edge devices aim to increase the camber of the airfoil in order to shift the liftslope, resulting in higher lift coefficients at the same angle of attack. Leading edge devices allow higher angles of attack by adjusting the camber to the stagnation point and thus delaying leading edge separation. Both result in an increase of the maximum achievable lift coefficient, referred to as $\Delta C_{l,flap}$ and $\Delta C_{l,droopnose}$ in the following. The reference maximum lift coefficient is defined by

$$C_{L,ref,max} = C_{L,clean,max} + \Delta C_{L,flap} + \Delta C_{L,droopnose} \tag{3.9}$$

For the determination of required section lift coefficient $C_{L,required}$, the advanced Diederich method, described in 3.5 is used. The remaining lift difference must be provided by the CCW system

$$\Delta C_{L,CCW} = C_{L,required} - C_{L,ref,max} \tag{3.10}$$

The lift gain by the circulation control can be expressed as a quotient of blowing coefficient and lift gain factor (LGF).

$$\Delta C_{L,CCW} = \frac{LGF}{C_\mu} \tag{3.11}$$

where C_μ is the blowing coefficient

$$C_\mu = \frac{\dot{m} V_{jet}}{\frac{1}{2}\rho_\infty V_\infty^2 S} \tag{3.12}$$

$$P_{cmp} = \dot{m}_{jet} cp (T_{tot,cmp,out} - T_{tot,cmp,in}) \tag{3.13}$$

The LGF is dependent on the desired section lift coefficient and is calculated by interpolation of data obtained from wind tunnel experiments [10]. Circulation control requires high mass flow and relative low pressure ratio for which axial compressors are most suitable. The required compressor power is : $P_{cmp} = \dot{m}_{jet} cp (T_{tot,cmp,out} - T_{tot,cmp,in})$. The compressor mass is then calculated according to interpolated data obtained by existing axial flow compressors, resulting in an compressor mass of 639 kg. The resulting CCW parameters are shown in table 3.11.

Table 3.11: High lift takeoff and landing settings

Parameter	Takeoff	Landing	Unit
$FlapSetting$	20	40	°
C_L	1.9	3.55	-
$\Delta C_{L,flap}$	0.47	0.7	-
$\Delta C_{L,droopnose}$	0.4	0.4	-
$\Delta C_{L,CCW}$	2.8	4.011	-
P_{comp}	1.11	1.39	MW
c_μ	0.026	0.0411	-

3.5.3 Tank Sizing

The mass of the tank system is the sum of all components. The structural mass is determined by calculating the minimum required wall thickness with an safety factor of 2.

$$t_{wall} = p_{max} \cdot D_{tank}/(4 \cdot \sigma_{allow}); \tag{3.14}$$

Aluminum is chosen as the structural material because of the low hydrogen embrittlement and good experience for cryogenic hydrogen tank. The insulation thickness is set to 0.2 m, which is sufficient to reduce the heat input and thus realize adequate holding times.[24] The mass of structure and insulation is then calculated with the material densities and volumes. Linear interpolation of similar existing systems is used to derive the mass of fuel lines and pumps.

Table 3.12: Tank parameters

Parameter	Value	Unit
p_{max}	1.5	bar
m_{H2}	1,222	kg
V_{H2}	17.45	m^3
t_{ins}	0.2	m
$t_{structure}$	0.005	m
$m_{structure}$	312	kg
$m_{insulation}$	196	kg
$m_{linesandpumps}$	293	kg
m_{total}	802	kg
η_{grav}	0.604	-

3.5.4 Stabilizer Sizing

The tailplane is calculated using Torenbeek's method [36]. Here, the area of the tailplane is calculated via a volume coefficient, the wing area and the lever arm. For the volume coefficient of the tail unit, a similar configuration must be considered, with similar Mach number, engine arrangement, position of the wing, sweep and tail unit configuration. Here, the first guess is made with this estimation method and in the iteration, the tail is tuned more precisely by determining the centre of gravity. There the lever arm is obtained by calculating the wing and tail neutral point, which results in the required moments. In this way, the required tailplane area is further optimised with each iteration step.

3.6 Structure & Stress

In order to reduce the structural mass of the high aspect ratio wing, the wing is supported by a strut attached to the fuselage. In addition to the high aspect ratio, a thinner airfoil can be used for minimizing the zero drag coefficient and therefore increasing the efficiency even more. Since there are no fuel tanks included in the wing box, the structure is not limited by the need of space to carry the fuel. This has two effects on the wing structure. In positive load condition i.e the 2.5g load maneuver, the relieving load caused by the fuel weight in conventional aircrafts is not present, which makes this load condition even more critical, here the strut braced wing can counteract this disadvantage. The second effect is on the taxi bump load condition (2g). In this load condition, there is no lift present and the wing is exposed only to its weight. Especially for high aspect ratio wings it is critical due to the high weight of the fuel contained in the wing, with no lift force to counteract, there is a risk, that the wingtips touch the ground while taxiing. Because there is no fuel present in the wing, this load condition is not as critical as for conventional kerosene powered aircraft. The strut braced wing configuration applied, consists of a strut and an offset piece, to reduce aerodynamic interference with the wing. The offset piece is fixed to the wing and pin joined to the strut, which is on its part pin joined to the fuselage. The weight of the strut would drastically increase when taking into account compressive forces and buckling. To avoid this, the strut is designed as a telescopic sleeve, in this way it is only subjected to tension loads, taking full advantage of the high tensile strength of carbon fiber reinforced plastics.[37] In negative load conditions and the taxi bump load condition the strut is inactive. Furthermore, to reduce fatigue a slack load factor is introduced, so that the strut engages until a certain load factor. Thereby it will be inactive in cruise condition, so repeated stress due to gusts in cruise can be avoided. Due to the vertical offset, the offset piece is subjected to tension and bending, so its weight will increase drastically when increasing the strut force and the offset length.[38] The wing box is adopted as a two-plate model, so only bending and no torsion is taken into account. The shear force, bending moment curves and wing deformation are calculated according to the beam theory. [39] The wings load distribution is assumed to be elliptical. By integration of the wing load along the span, with the engine weight and vertical strut
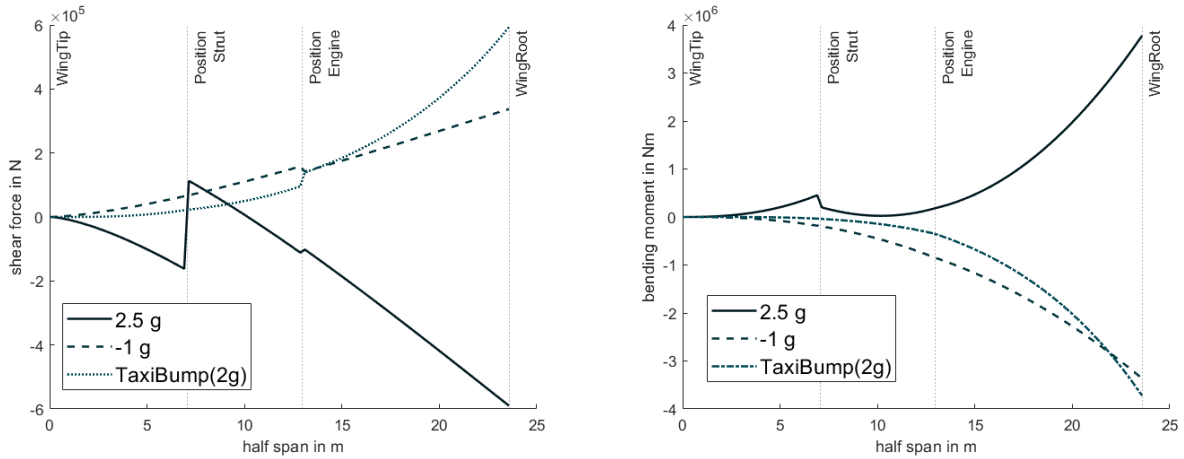
Figure 3.10: Shear force and bending moment over span

force, the shear force is obtained. (see Figure 3.10 Equation 3.18 is the integration of shear force and additionally taking into account the horizontal strut force, creating an relieving constant moment, which can be observed in the moment plot.

$$q(y) = 2 \cdot MTOM \cdot g \cdot n_z \cdot \frac{\sqrt{(\frac{b}{2})^2 - (\frac{b}{2} - y)^2}}{\frac{b}{2} \cdot 2 \cdot \pi} \tag{3.15}$$

In a first step, the panel thickness distribution is obtained by the fully stressed criterion, for both load cases. Where the upper envelope builds the absolute minimum required panel thickness. The wingtip displacement can be calculated with

$$w(tip) = \int \frac{2 \cdot M \cdot y_i}{E_1 \cdot c_b \cdot t_m \cdot d^2}(0 - \frac{b}{2}) \tag{3.16}$$

The panel thickness is then increased iterative at certain positions, so that the tip displacement is equal to the maximum allowed tip displacement, which is set to 20 % of half wingspan. the resulting thickness distribution, as well as the thicknesses obtained from the fully stressed criterion, are shown in figure (thickness distribution). From there, the wing slope and deflection can be calculated using the first and second integral of $w'' = \frac{M_b}{E \cdot I}$

$$V(y) = -\int_0^y q(y)dy + W_e \cdot u(y - y_e) + F_{sv} \cdot u(y - s) \tag{3.17}$$

$$M_b(y) = -\int_0^y V(y)dy - F_{sh} \cdot L_{off} \cdot u(y - s) \tag{3.18}$$

$$w'(y) = -\int_0^y \frac{M_b(y)}{E \cdot I(y)}dy \,;\, w = -\int_0^y w'(y)dy \tag{3.19}$$

The design variables of the strut braced wing are the offset length, strut position and the strut force. Those are varied through the optimization process. An optimum is found when the strut and wing masses become minimal, while the wing tip displacement remains within the range of allowable deformation. The wing bending mass is calculated using the volume obtained by the panel thickness calculation and the material density. The mass of the remaining components like leading and trailing edge devices, ribs, stringers and wing skin is then calculated according to FLOPS equations. The mass of strut and vertical offset piece is calculated according to the equations in [37]. Since the variable parameters i.e offset length, strut position and strut force lead to party opposing effects on weight and additionally drag, an optimization tool is used to find the global minimum.
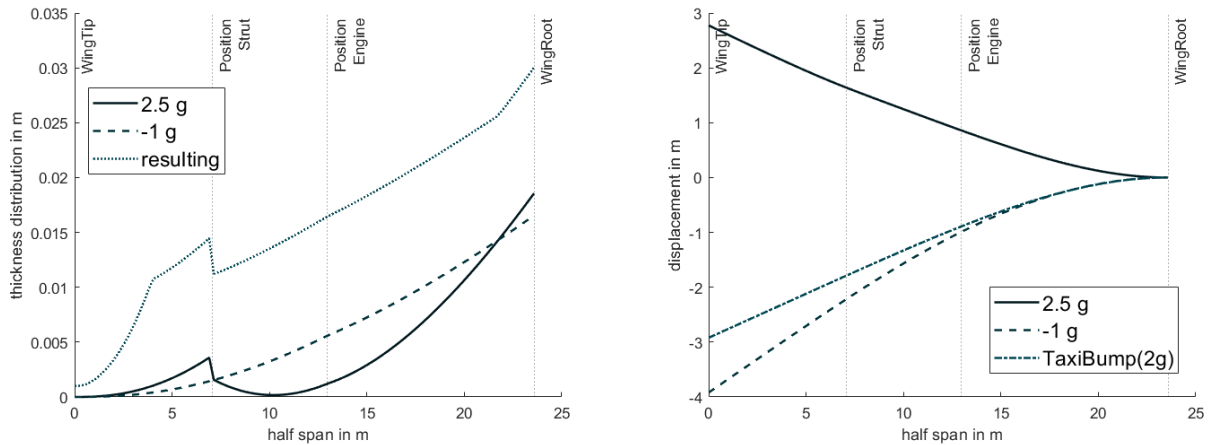
Figure 3.11: thickness distribution and wing displacement over span

3.7 Weight & Balance

Based on the given requirements and the resulting configuration, various masses are obtained using the estimation methods of [40] and [41]. The methodologies are empirical estimation formulas that were applied to standard components. As shown in the previous chapters, components that are not part of the standard aircraft were calculated using methods tailored to them separately. The combination of those then provides the total mass for CHANGE and will be more optimized with every iteration loop.

The airframe structure includes the fuselage, the strut-braced wing, tail group, tank as well as the landing gear, high lift devices and rudders. These add up to a total frame mass of $20,851\,\mathrm{kg}$.

The powertrain includes more than just an internal combustion engine. With the chosen concept of a fuel cell powered aircraft, the mass proportion of the powertrain increases and with it the operating empty mass (OEM). The mass of the powertrain is made up of two main components. The power generator and the power consumer respectively the propulsion unit. This includes the integration of both systems in the aircraft. Those two components, together with the associated electronics and wiring, result in a powertrain mass of $20,188\,\mathrm{kg}$.

All remaining parts of the OEM are combined here in service & equipment and operational items. The heaviest items are air conditioning and anti-ice, as well as more electronics for cabin systems and avionics. These are closely followed by cabin supplies, safety equipment, passenger seats and, finally, operational components of the cockpit. Altogether, this results in a mass of $14,895\,\mathrm{kg}$.

The payload mass is set at $15,750\,\mathrm{kg}$ by the specification of the PAX and their luggage. The fuel mass determination will be explained with the fuel fraction method after Roskam [42] in chapter 3.9 and adds $1,147\,\mathrm{kg}$ to the total mass of the aircraft. It is striking that the fuel mass only accounts for $1.6\,\%$ of the total mass. This makes the difference between maximum take-off mass (MTOM) and maximum landing mass (MLM) very small. The reason for this is the configuration of the aircraft 2 or the powertrain with fuel cells 2.3. As a result, the OEM also takes up a relatively large share of the total mass and the maximum zero fuel mass (MZFM) is relatively large at $72,831\,\mathrm{kg}$. This can also be seen in the pie chart E.1.

The main landing gear is mounted in a belly fairing below the fuselage for stability and weight reasons. The position was determined in compliance with the required clearance angle and rotatability and is at $28\,\mathrm{m}$ from the nose of the fuselage. Furthermore, the centre of gravity calculation with the component groups from the figure in Appendix E.1 results in a stability measure of $5\,\%$.

3.8 Detailed Drag

In order to be able to make a well-founded statement about the drag and thus also about the L/D ratio, the drag has been split into the following elements see Table 3.13. and investigated on the

influence for varying lift coefficients (according to Diederich [35]).

Table 3.13: Detailed drag

Element	Description
Drag vertical stabilizer	Drag due to friction
Drag horizontal stabilizer	Drag due to friction
Drag trim	Induced drag due to changing lift
Drag downwash	Drag due to wing downwash
Drag interference	Interference drag from transitions of wing, nacelle, stabilizers and fuselage
Drag fuselage	Drag due to friction
Drag engine nacelle	Drag due to friction
Drag wing	Drag due to friction
Drag induced	Induced drag of wing
Drag transsonic	Drag due to compressibility
Drag strut	Drag due to friction

Drag wing airfoil   The drag coefficient for the entire wing is obtained with Equation (3.20) by integrating the local foil drag coefficient over the dimensionless half span.

$$C_{D_{wing}} = \int_{\eta_{fuselage}}^{1} C_{D,a}(\eta) \cdot \frac{l(\eta)}{l_m} \, d\eta \tag{3.20}$$

Drag wing induced   The additional drag due to tip twist is also accounted for when calculating the induced drag with Equation (3.21).

$$C_{D,i} = c_2 \cdot \frac{C_{L,W}^2}{\pi \cdot \Lambda} + c_1 \cdot C_{L,W} \cdot \Delta\epsilon + c_0 \Delta\epsilon^2 \tag{3.21}$$

$$\tau = 1 - \Lambda \cdot (0.002 + 0.0084 \cdot (\lambda - 0.2)^2) \tag{3.22}$$

$$c_0 = c_{L_a}'^2 \cdot (0.0088 \cdot \lambda - 0.0051 \cdot \lambda^2) \cdot (1 - 0.0006 \cdot \Lambda^2)$$

$$c_1 = c_{L_a}' \cdot d(0.0134 \cdot (\lambda - 0.3) - 0.0037 \cdot \lambda^2)$$

$$c_2 = {}^1\!/_\tau \left(1 + 5 \cdot 10^{-6} \cdot d \left(\frac{|\varphi_{25}|}{1°} \right)^3 \right)$$

Drag transsonic   With Equation (3.23) the transsonic drag due to compressibility losses is calculated based on the Drag-Divergence Mach number (Ma_{DD}).

$$\Delta C_{D,Ma} = 0.002 \cdot e^{(60 \cdot \Delta Ma)} \tag{3.23}$$

$$\Delta Ma = Ma_{CR} - \frac{Ma_{DD}}{\sqrt{(cos\varphi_{25})}}$$

Drag fuselage   In Equation (3.24) The fuselage drag considering pressure drag is approximated according to a flat plate. The circulation is assumed to be fully turbulent.

$$C_{D,f} = C_{fr,tu} \cdot (1 + k_f) \cdot \frac{S_{wet}}{S_{wing}} \tag{3.24}$$

$$C_{fr,tu} = \frac{0.455}{(logRe)^{2.58}}$$

$$k_f = 2.2 \cdot \left(\frac{D_f}{l_f}\right)^{3/2} + 3.8 \cdot \left(\frac{D_f}{l_f}\right)^3$$

Drag engine nacelle Apart from the pressure drag factor, $k = 0.2$, the drag deriving from the engine nacelle is calculated equivalent to the fuselage drag.

Drag stabilizers For the stabiliters only the parasitic drag is accounted for while the induced drag is neglected. Horizontal and vertical stabilizers are calculated equally, but with the corresponding geometrical parameters.

$$C_{D,S} = 2 \cdot C_{fr,s} \cdot (1 + k_s \cdot cos(\varphi_{50})^2) \cdot \frac{S_s}{S_{wing}} \tag{3.25}$$

Drag trim Trim drag is defined as the induced drag due to the change in lift of the vertical stabilizer, to trim the airplane. This drag can be calculated using Equation (3.26) with τ_{hs} analog to Equation (3.22).

$$C_{D,trim} = \frac{C_{L,hs}^2}{\pi \cdot \Lambda_{hs} \cdot \tau_{hs}} \cdot 1 + 5 \cdot 10^{-6} \cdot d\left(\frac{|\varphi_{25,hs}|}{1°}\right)^3 \cdot \frac{S_{hs}}{S_{wing}} \tag{3.26}$$

Drag downwash The downwash of the wing crates additional drag on the horizontal stabilizer calculated with Equation (3.27), downwash angle α_w and dynamic pressure ratio $\frac{q_{hs}}{q} = 1$ for T-tail configuration.

$$\Delta C_{D,hs} = C_{L,hs} \cdot sin(d\alpha_w) \cdot \frac{q_{hs}}{q} \cdot \frac{S_{hs}}{S_{wing}} \tag{3.27}$$

Drag interference The interference drag is approximated with Equation (3.28). Where n is the number of similar intersections of subassemblies and l_{int} the length of this intersection.

$$C_{D,int} = \sum_{i=1}^{m} \frac{(C_{D,int} \cdot f_s)_i}{S_W} \tag{3.28}$$

$$(C_{D,int} \cdot f_s)_i = \frac{0.1369}{Re^{0.4}} \cdot l_{int}^2 \cdot n$$

These results, the drag coefficients for different elements are displayed cumulatively in Figure 3.12. For a cruise lift coefficient of $C_{L,cruise} = 0.44$ and a corresponding $C_{D,cruise} = 0.0171$ the $^L/D_{cruise}$ ratio equals 25.7 . With these parameters the cruise Mach number and cruise altitude the thrust at cruise totals 27.72 kN.

3.9 Mission Analysis

All calculations performed in previous chapters must lead to a result in the design point. To check, if this point is achieved, calculated values for all flight phases are used. For every mission phase as seen in 3.13, the data has to be checked if it is sufficient. Additionally the overall necessary energy is calculated according to performance data to evaluate the fuel cell efficiency accurately and check the previously calculated fuel masses. The energy calculation separates the climb phase into three sections. Thereby a more exact calculation of needed fuel can be made. The climb is not separated in different sections because the loss of mass during flight is very small due to the high energy density of LH2. The descend is assumed as not fuel consuming, because the needed amount of energy in this flight segment is very small.

Additionally to this method based on flight mechanics, the fuel fraction method after Roskam [42]
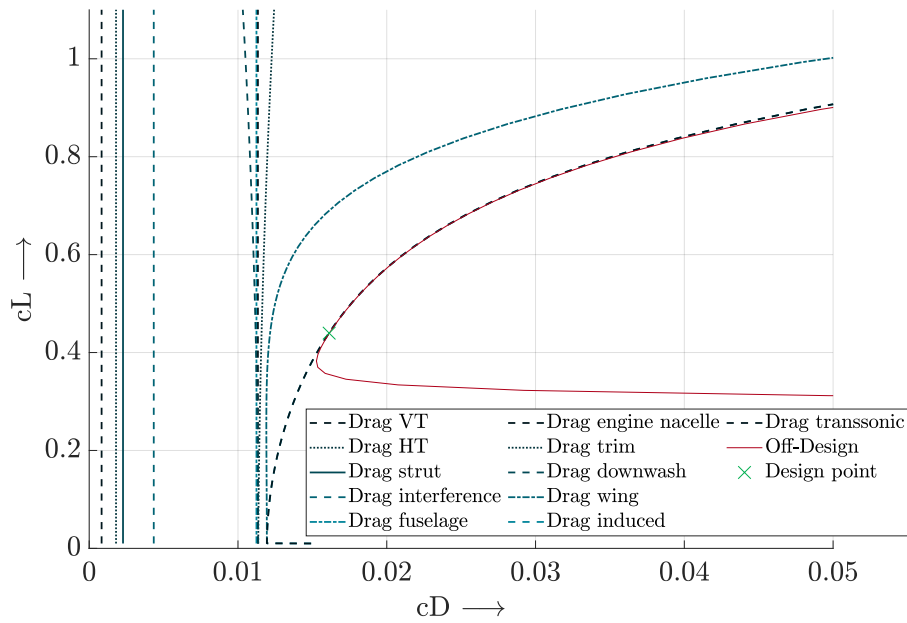
Figure 3.12: Cumulative drag

Figure 3.13: Mission profile

is used as well do check the calculated values. It is based on the range equation by Breguet and enables a more accurate consideration of mass-changes during longer flight phases. Based on the low fuel consumption, the two methods were found to give almost equal results but provided good capability of verification of the overall design process.

If the values are converging and the design range can be reached, a cost analysis follows. Else, the iterational process needs to start over.

3.10 Cost Analysis

The cost analysis follows the method of J. Thorbeck [43]. It is a simplified analysis of DOC which includes factors such as fuel prices, salaries, maintenance and fees. Therefore the DOC is split into route independent costs and route dependent costs. The independent costs are roughly estimated by a price per kg OEM and other variables like interest rate for loans as well as the crew salaries. For their calculation market standards has been chosen as values. The route dependent costs are mostly influenced by the expected flight cycles per year and the according range. These calculations lead to DOC and SKC, where the DOC is applied onto the seat kilometer offered. The overall goal is to achieve a as low as possible SKC and makes it to the main optimization parameter. The result per calculation are fed into the optimization algorithm to determine the best detailed design.

4 Evaluation

This section is meant to take a closer look on the results of the simulation workflow and how they could be interpreted. This will lead in a closer look at costs, the comparison between CHANGE and a choosen reference aircraft as well as the handling in terms of operations in reality.
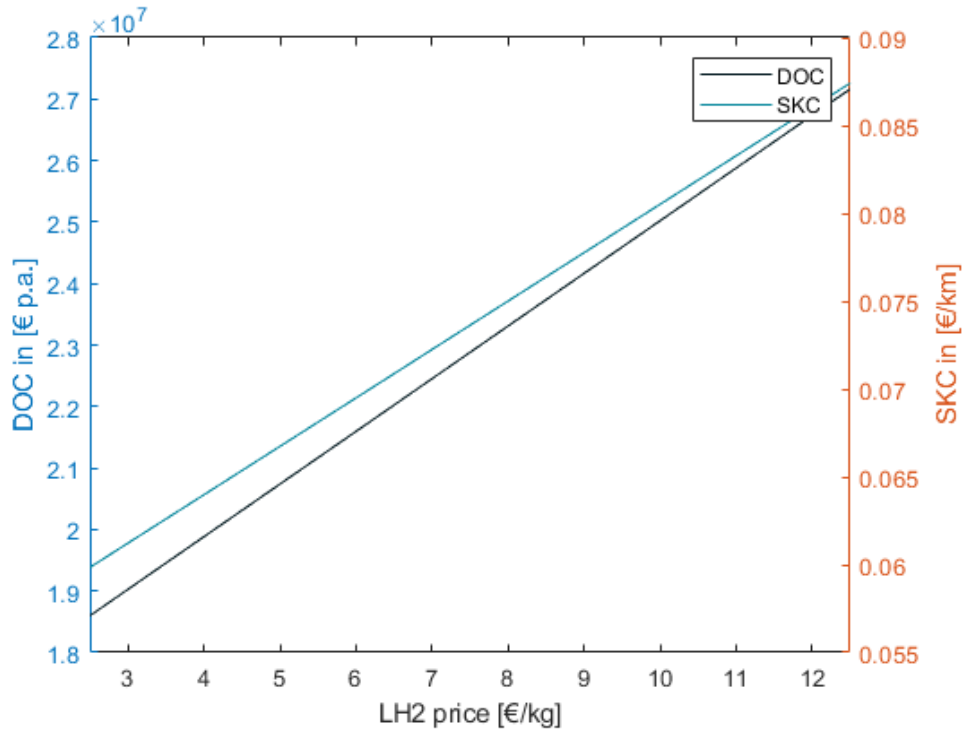
4.1 Costs

Figure 4.14: Operating Cost over LH2 price

The operating costs are one of the most important factors for airlines, when choosing to buy an aircraft. To estimate these, a simplified method after J.Thorbeck [43] has been used to provide the necessary comparability. Calculated values are shown in 4.14. Included in the DOC calculation for the A220-300 is a CO2-tax for jet fuel. The fuel price is chosen as a current market value of $600\,^{EUR}/\mathrm{t}$ for JET A1 and $1,000\,^{EUR}/\mathrm{t}$ for SAF [44].

A CO_2 tax has been included in the fuel price in the DOC calculation with a price of $100\,^{EUR}/\mathrm{t}$ CO_{2eq} by 2035 as estimation met through current political discussions and current developments.[45] According to current EASA assessment, the carbon dioxide emissions emitted by jet engines can be approximated with $40\,\%$ of the total amount of CO_{2eq} so $3.15\,\mathrm{kg}\ CO_2$ per kg JET A1. The remaining $60\,\%$ are approximated with are additional $4.725\,\mathrm{kg}\ CO_{2eq}$ per kg JET A1. Thus, the CO_2 tax of the EU have been calculated as the CO_2-Emmision plus additional $150\,\%$ to include non-CO_2-emission to receive a realistic total for the fossil fuel portion. The SAF portion of GHG emissions is assumed as $67\,\%$ in comparison to fossil fuel [46]. The price for LH2 has been evaluated with a value of This value is a current market price to provide a comparability between the reference aircraft and CHANGE. With a view to the current and future market situation a lower price for LH2 and a higher jet fuel price are imaginable, but it is not possible to evaluate these. An advantage of the LH2 fueled CHANGE is, that the complete supply chain is able to use renewable green energy and can be propelled by LH2. Thereby, no GHGE are to be expected and thus, no CO2 taxes as well. This economical advantage is not possible to evaluate from today's view too. The influence of the LH2 price onto the DOC is shown in 4.14.

Table 4.14: Comparison of DOC

		CHANGE		A220-300	
		2,000 km	600 km	2,000 km	600 km
DOC in $\text{EUR}/\text{p.a.}$		24,592,000	21,703,000	19,519,000	15,408,000
SKO in km · Seats offered p.a.		310,770,000	93,232,000	336,020,000	100,810,000
SKC DOC/SKO in EUR	=	0.079	0.233	0.059	0.156
CFK in EUR/km		11.87	34.92	8.86	23.44

Because of both possible price developments, the SKC as seen in 4.14, which is 25 % apart from each other, could progress to converge until the EIS 2035. This leads to the assessment that an operation of change in mass production with sufficient users would be economically possible. Additionally, it is to consider, that the environmental awareness in the worldwide population is growing. Thereby, a customer might be more likely to fly with a „green" aircraft and thus aggregate more demand for „green" aviation and the airlines offering those.

4.2 Comparison with Reference Aircraft

The selected reference aircraft is to be considered and compared directly with CHANGE. After extensive literature research, the A220-300 was chosen as the reference aircraft. This was based on various factors.

Table 4.15: Data Sheet Table

Designation	CHANGE	A220-300
Overall Length in m	40.16	38.69
Overall Height in m	9.04	11.47
Wing Span in m	47.15	35.08
Wing Area in m^2	133,1	112.3
Wing Loading in N/m^2	5,784	5,364
Energy Consumption RP in MJ	143,344	246,645
Average Climb Rate in m/s	11.5	12.7
Cruise Mach number in 1	0.70	0.78
Cruise Altitude in m	8,000	14,000
MTOM in kg	72,831	58,502

The most important selection criterion was an aircraft that can carry the same payload. Furthermore, the reference aircraft should be as technologically advanced as possible. This ensures that when the aircraft enters service in 2035, it will not be an outdated and inefficient aircraft. Also, the reference aircraft should be in the same weight class as the comparison aircraft. Unfortunately, these selection criteria eliminate all comparable civilian propeller-driven aircraft currently in service. As a result, CHANGE has to be compared with a turbofan-powered aircraft, which means that the cruise mach number and the cruise altitude are not identical.

However, after extensive research by the authors, the A220-300 is the most useful comparison for CHANGE. To further improve the comparability, both aircraft are compared in a reference point (RP). The RP is set to a mission with 150 PAX and a flight mission of 2,000 km including safety margin, which corresponds to the requirements. In the 4.15 table, the most important data of CHANGE were brought together and can now be directly compared with the A220-300. It is important to note that the reference aircraft is loaded for the identical mission (150 PAX & 2,000 km + safety margin) and both aircraft fly with their own mission profile. Thus, the reference aircraft does not fly in the design point, but it is directly comparable with CHANGE. The pie chart E.1 shows that the mass distribution of a hydrogen-powered aircraft increases significantly for the OEM. The powertrain group is mainly responsible for this. However, the fuel mass is significantly reduced, as very little

fuel mass is needed due to the high energy density of LH2. In the figure E.2 the payload-range diagrams of CHANGE and the A220-300 are plotted in a single diagram. As can be seen, the maximum payload of the A220-300 is higher. However, additional cargo transport is possible and intended for the reference aircraft. Thus, the maximum loading capacity in terms of PAX is almost identical for both aircraft and therefore well comparable. Moreover, in the case of CHANGE there is no substitution of the PAX by additional fuel, since the fuel mass fraction of a hydrogen-powered aircraft is too low for this.
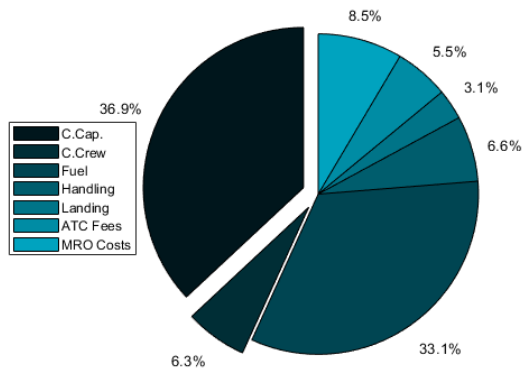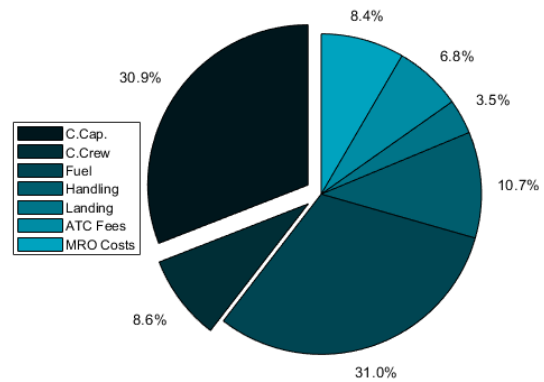

Figure 4.15: DOC CHANGE

Figure 4.16: DOC A220-300

In the two figures 4.15 & 4.16 and in table 4.14, it can be seen that CHANGE is currently still significantly more expensive than the comparison aircraft. However, relative cost items such as fuel may decrease in the near future due to better infrastructure for LH2, as can be read in 1.2 and 4.1. Furthermore, the fuel costs for the reference aircraft would be increased by a tendency to increase the taxation of CO2. This could lead to an equalisation of costs. The chapter 4.1 goes into more detail on how the costs break down to date.

Table 4.16: Flight Mission Energy Consumption A220-300

Mission Segment	Length in km	Fuel consumption in kg	Energy in MJ [47]	GHG emissions in kg CO_{2eq}
Commuter Mission	600	1,852	80,560	13,126
Commuter Mission plus Safety	1,300	3,821	166,213	27,081
Design Mission	2,000	3,783	164,560	26,812
Design Mission plus Safety	2,700	5,670	246,645	40,186

From the comparison of the total energy consideration of both aircraft in table 4.16 & 4.17, it can be seen that CHANGE clearly outperforms the A220-300 in total energy consumption. This means that in the future, the energy consumption for hydrogen aircraft like CHANGE is significantly lower than for a similar aircraft flying using Jet A1 or Sustainable Aviation Fuel. This consideration shows that it is more energy-efficient to fly with hydrogen aircraft. Therefore, in the future, with optimised processes and infrastructure, it may even be possible to fly more cheaply than today with conventional fuel.

Also in the emissions, CHANGE is ahead of the reference aircraft by a huge margin as shown in the tables 4.16 & 4.17. Because of the installed fuel cells in combination with the "low" flight altitude of 8,000 m, no influence on the atmosphere by CO2 equivalents is measurable, as already described in the introduction to 2. Thus, CHANGE is already very well prepared for the requirements of Flightpath 2050 in 2035.

4.2.1 Comparative Energy Analysis

To evaluate the concept a comparative energy analysis follows. According to the assignment definition, the overall efficiency to provide LH2 is calculated as following:

$$\eta_{overall} = \eta_{origin} \cdot \eta_{electrolysis} \cdot \eta_{LDS} = 0.672 \tag{4.29}$$

Thereby, the overall required energy for CHANGE for the design mission is:

$$E_{req} = \frac{E_{LH2,chem}}{\eta_{overall}} = \frac{103,923\,\text{MJ}}{0.672} = 154,647\,\text{MJ} \tag{4.30}$$

And for the 600 km mission :

$$E_{req} = \frac{E_{LH2,chem}}{\eta_{overall}} = \frac{36,786 MJ}{0.672} = 54,741\,\text{MJ} \tag{4.31}$$

The A220-300 as reference aircraft is fueled by a mix of 70 % jet A1 and 30 % SAF. For the SAF an oil palm based fuel has been chosen, because it has the highest potential of being produced in a high volume [48]. Therefore, the energy efficiency for both fuels has been calculated as following:

$$\eta_{ffuel} = \eta_{cox} \cdot \eta_{cot} \cdot \eta_{ref} \cdot \eta_{distr} = 0.952 \cdot 0.991 \cdot 0.922 \cdot 0.996 = 0.866 \tag{4.32}$$

$$\eta_{SAF} = \eta_{coop} \cdot \eta_{eoc} \cdot \eta_{toc} \cdot \eta_{prod} \cdot \eta_{distr} = 0.917 \cdot 0.513 \cdot 0.995 \cdot 0.893 \cdot 0.996 = 0.416 \tag{4.33}$$

The efficiency of the fuel mixture is:

$$\eta_{total} = \eta_{SAF} \cdot 0.3 + \eta_{ffuel} \cdot 0.7 = 0.696 \tag{4.34}$$

Thereby, for the design mission the following amount of total energy is required:

$$E_{req} = \frac{E_{fuel,chem}}{\eta_{overall}} = \frac{164,560\,\text{MJ}}{0.696} = 236,437\,\text{MJ} \tag{4.35}$$

Additionally, the amount for the 600 km mission:

$$E_{req} = \frac{E_{fuel,chem}}{\eta_{overall}} = \frac{80,560\,\text{MJ}}{0.696} = 115,747\,\text{MJ} \tag{4.36}$$

Through the production process, the following emissions are dispersed:

$$GHGE_{FFuel} = 11 \cdot \frac{gCO_2eq}{MJ_{out}} \tag{4.37}$$

$$GHGE_{SAF} = 40 \cdot \frac{gCO_2eq}{MJ_{out}} \tag{4.38}$$

In this values, the positive impact of photosynthesis by plants is not considered.

Identifiable is the nearly similar efficiency of the chosen supply chains. Even though, the overall aircraft efficiency of the CHANGE is significantly higher then the efficiency of the jet engine driven A220-300 because of the limited efficiency of jet engines. Furthermore, if the SAF share of the overall fuel mixture would increase above 30 %, the efficiency of the supply chain for jet fuel would decrease accordingly, making the overall needed energy amount significantly higher. As long term solution the production of SAF would have to become more efficient to compete further with LH2 driven aircraft. Especially if the efficiency of LH2 production would increase and get cheaper by higher demand and developing technology.

4.3 Operational Design

This subchapter takes a closer look at various areas of operational design. This includes, for example, the handling on the ground in terms of turn-around time. Furthermore, cases of error and how to deal with them are discussed, as well as fuel and energy consumption in the respective flight phases of CHANGE.

4.3.1 Ground operations

The general ground operation concept is meant to fit today's airports and pre-existing infrastructure. According to the requirements specification, the aircraft fits the ICAO Aerodrome Reference Code 4-D with a takeoff field length of $2,000\,$m and a wingspan of $47.15\,$m. Because of the electric engines, no idle running before takeoff is necessary. To increase fuel economy and reduce noise emissions, a small electric nosewheel motor is installed for taxiing at the airport before takeoff and after landing. The nosewheel motor offers the ability to reduce turnaround time and thereby handling fees, because no external pushback is required.

Refueling of LH2 tanks is comparable to conventional fuels with an approximated flow rate of about $900\,l/\text{min}$ [49] Thereby the estimated refuel time for CHANGE is about $13\,$min. Compared to the reference aircraft with an estimated refueling time of $10\,$min too, the loss of time in ground handling can be kept as small as possible. An uncertainty, which cannot be evaluated at the current point is, if it is possible to run parallel operations in ground handling during refueling. If not, the turnaround time is close to similar (dependent of the usage of two fuel hoses), but if during refueling boarding and deplaning of passengers is restricted, the ground handling time extends roughly by the time needed to refuel. Goal in the best case is a turnaround time oriented to the A220 with $20\,$min. The exact sequences of the ground handling are visualized in Appendix Appendix D.

The biggest difference occurs in reviewing the necessary infrastructure to supply the LH2. A new fuel depot, different fuel trucks and new safety guidelines are necessary to handle this propellant. These are challenges necessary to overcome for the use of LH2 and not excessive complex but a larger one-time expense. Due to the limited fuel volume in the aircraft, a LH2 supply is necessary in nearly every mission scenario.

Similar to how the APU is handled on a conventional aircraft the fuel cells can be handled. They are built modular on racks stored in the tail cone of CHANGE. To access them a maintenance door is built into the tail cone. The racks can be removed individually, to access the module for which maintenance is necessary. Thereby a change of the complete fuel cell portion is easily possible and comparable to today's aircraft power-plants.

4.3.2 Failure Handling Liquid Hydrogen

Due to the atmospheric separation of the aft section from the rest of the aircraft, there is no possibility of problems arising from the hydrogen outside this section. The largest thread is the buildup of an explosive atmosphere inside and surrounding the tank. Inside the tank the common concept to prevent this is an over-saturation of the tank by hydrogen gas. This is achieved by heating coils that maintain an over-pressure in the tank if the natural boil-off is no longer sufficient. The over-pressure prevents oxygen from entering the tank. For the outside of the tank the opposite tactic is used. In order to avoid large accumulations of potentially escaping hydrogen gas, the aft section is ventilated constantly. The constant used air mass flow from the cabin is used for this purpose. Furthermore, a hydrogen gas warning system is necessary to permanently monitor the hydrogen gas concentration in the aft section. In case of a high flow leaking event, ram air inlets can be used to increase the ventilation air flow. In case of a severe emergency event the hydrogen system provides the possibility to jettison the fuel.

4.3.3 Mission

Flight segments are broken down in tables 4.17 for the design mission and in 4.18 for the $600\,$km mission. CHANGE does not emit any GHGE because of the LH2 propulsion. No GHGs occure during the flight mission. In direct comparison the A220-300 as chosen reference aircraft powered by conventional fuels with a 30% SAF admixture emits $26,812\,$kg CO_{2eq}. The mission performance

calculation produced the results shown below in tables 4.17 & 4.18. For simplicity, in descent, it is assumed that there is no fuel consumption, during landing the CCW-system consumes power. The amount of energy and mass for „Trip" is calculated according to the CS-25 with 5 % additional fuel/energy for safety reasons.

Table 4.17: Flight Mission $2,000\,km$ CHANGE

Mission Segment	Length [km]	Time [min]	Fuel consumption [kg]	Energy [MJ]	GHG emissions [kgCO$_{2eq}$]
Take-Off	2	0.8	7	797	0
Climb	155	14	179	21,416	0
Cruise	1,640	123	634	75,860	0
Descend & Landing	203	25	5	900	0
$\sum$ Trip	2,000	113	825	103,923	0
Diversion	370	35	163	19,461	0
Holding	307	45	159	19,059	0
$\sum$ Total	2,677	218	1,147	143,344	0

Table 4.18: Flight Mission $600\,km$ CHANGE

Mission Segment	Length [km]	Time [min]	Fuel consumption [kg]	Energy [MJ]	GHG emissions [kgCO$_{2eq}$]
Take-Off	2	0.8	6	723	0
Climb	142	14	147	20,832	0
Cruise	255	19	94	13,343	0
Descend & Landing	203	25	5	900	0
$\sum$ Trip	600	60	252	36,786	0
Diversion	370	35	163	19,461	0
Holding	307	45	159	19,059	0
$\sum$ Total	1,277	140	574	69,500	0

The values show the overall good energy efficiency despite the high OEM. This efficiency opens the opportunity to extend the range of the aircraft through lengthening the LH2 tank and the fuselage. As in usual stretch versions of passenger aircrafts the flight dynamics are not likely to change much, thereby research to extend the range seems reasonable especially when reviewing the trip fuel in comparison to the contingency and diversion fuel, which get percentual smaller as the range increases.

5 Conclusion

CHANGE was able to prove that aviation with minimal climate impact is possible. The international aviation can take an important and necessary step toward a climate-neutral transport sector. Although currently comparable fossil-fuel powered aircrafts have lower operating costs than CHANGE, there is a high probability that this will change in the future due to increasing political pressure.

Appendix

Appendix A Technology Readiness Assessment

The following table provides an overview of the TRL of utilized technologies of CHANGE.

Table A.1: Evaluation of the Technical Readiness Level of utilized technologies

Component	TRL	Source
SBW	6	[50]
NLF	8	[51]
CCW	6	[52]
PEM Fuel Cells	8	[51]
CROR	9	[53]
Foam insulated hydrogen tanks	9	[54]
High Power Electric Motors	9	[26]

Appendix B Mission Analysis

Figure B.1: 2000km around Delhi Intl.

Figure B.2: 2000km around Frankfurt Intl.

Figure B.3: 2000km around JFK Intl.

Figure B.4: 2000km around Beijing Intl.
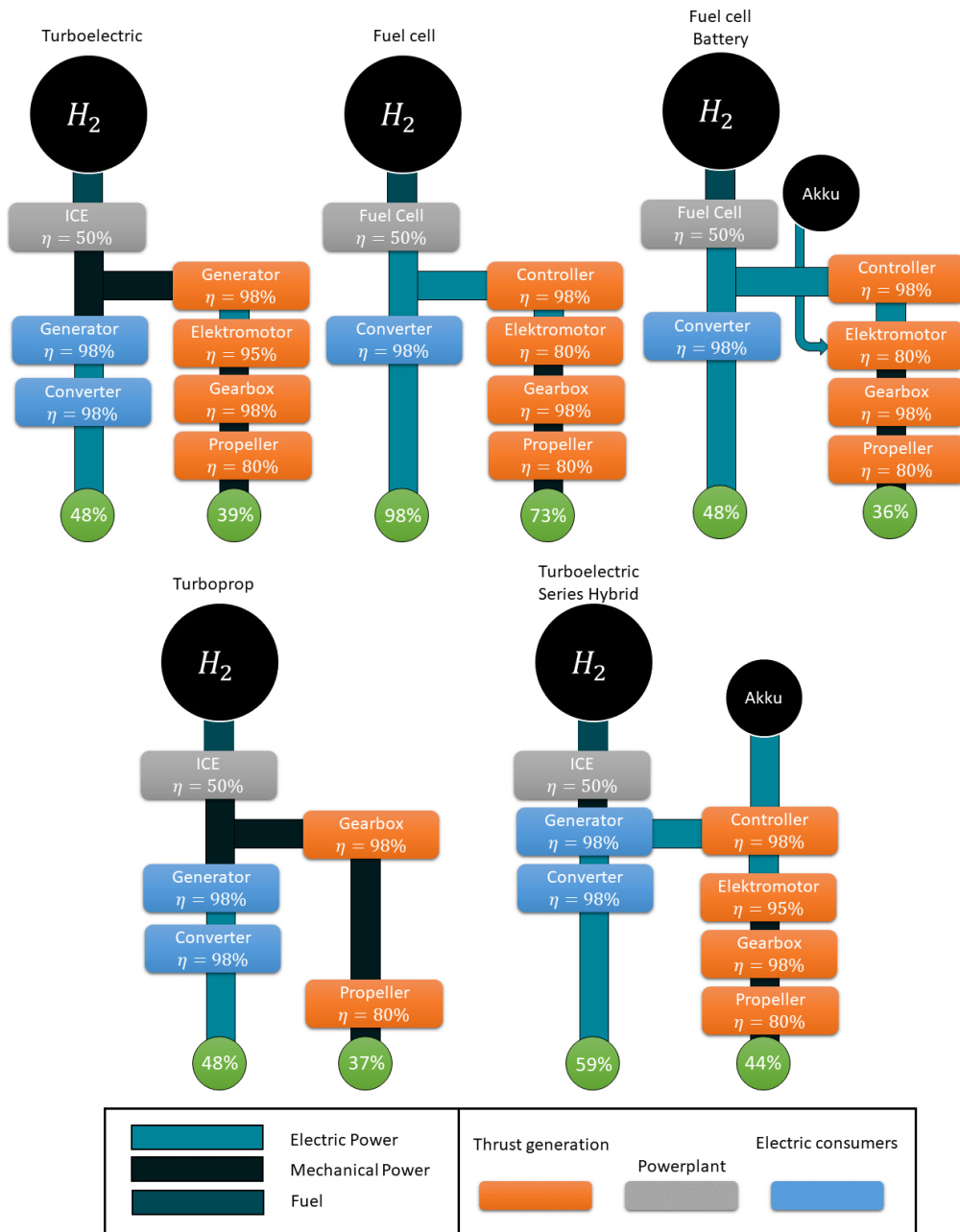
Figure C.1: Hydrogen fueled powertrain/propulsion concepts [55]

Appendix D Ground Operations
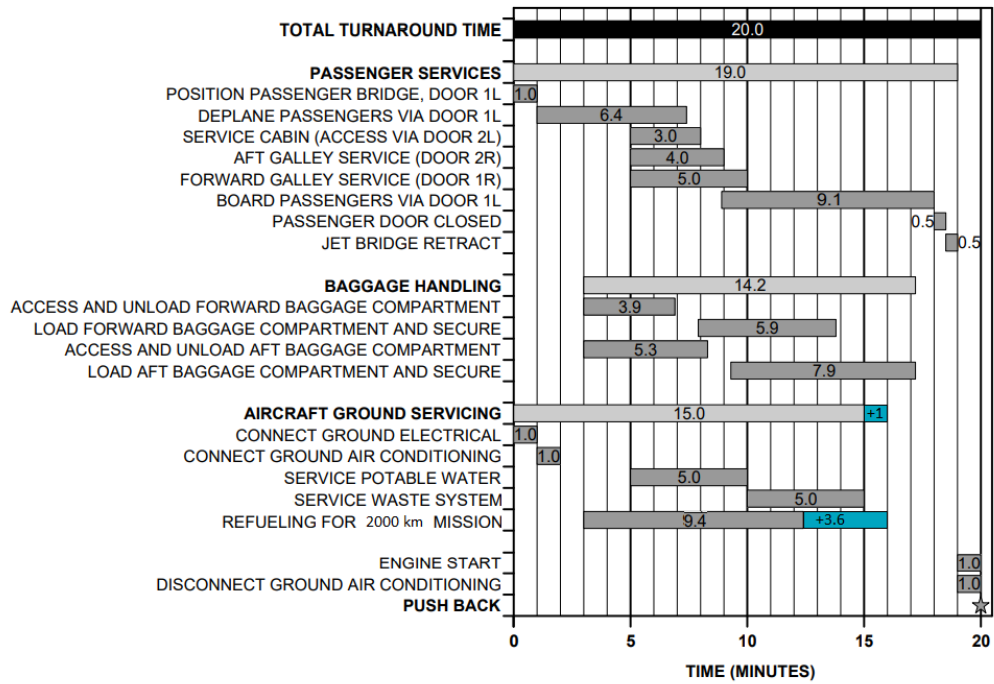
Figure D.1: Ground Handling Sequence for A220 and CHANGE. Blue - refuel time addition for CHANGE (edited figure according to [56])
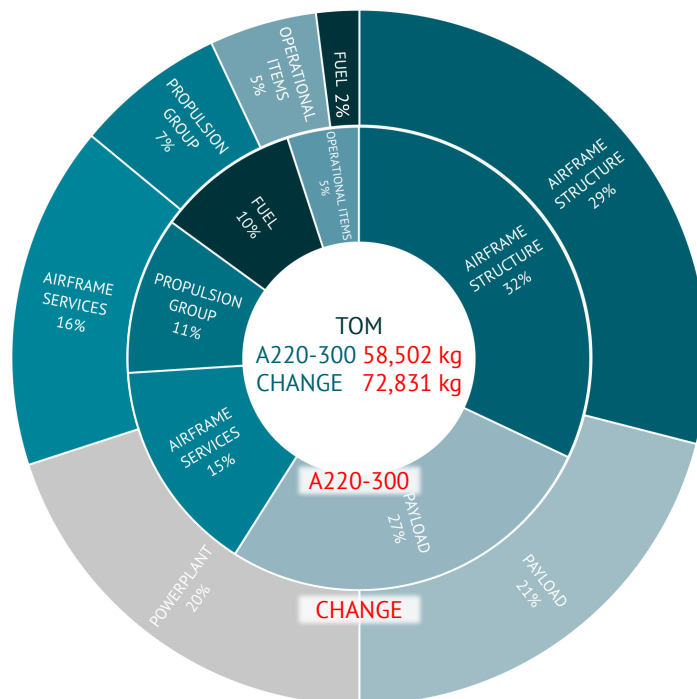
Appendix E Reference Aircraft

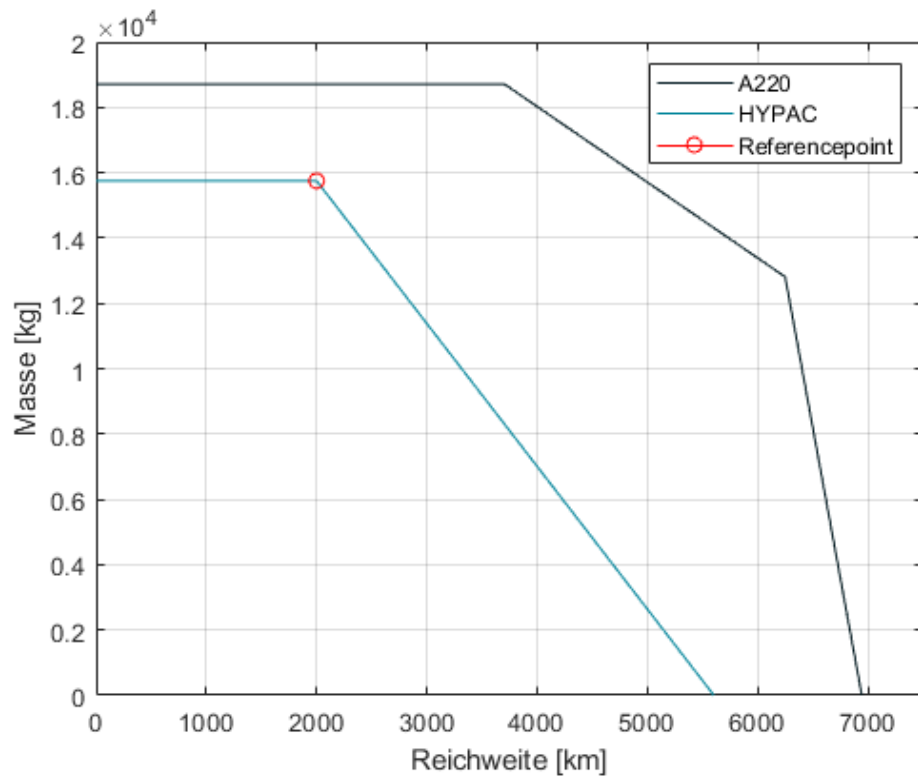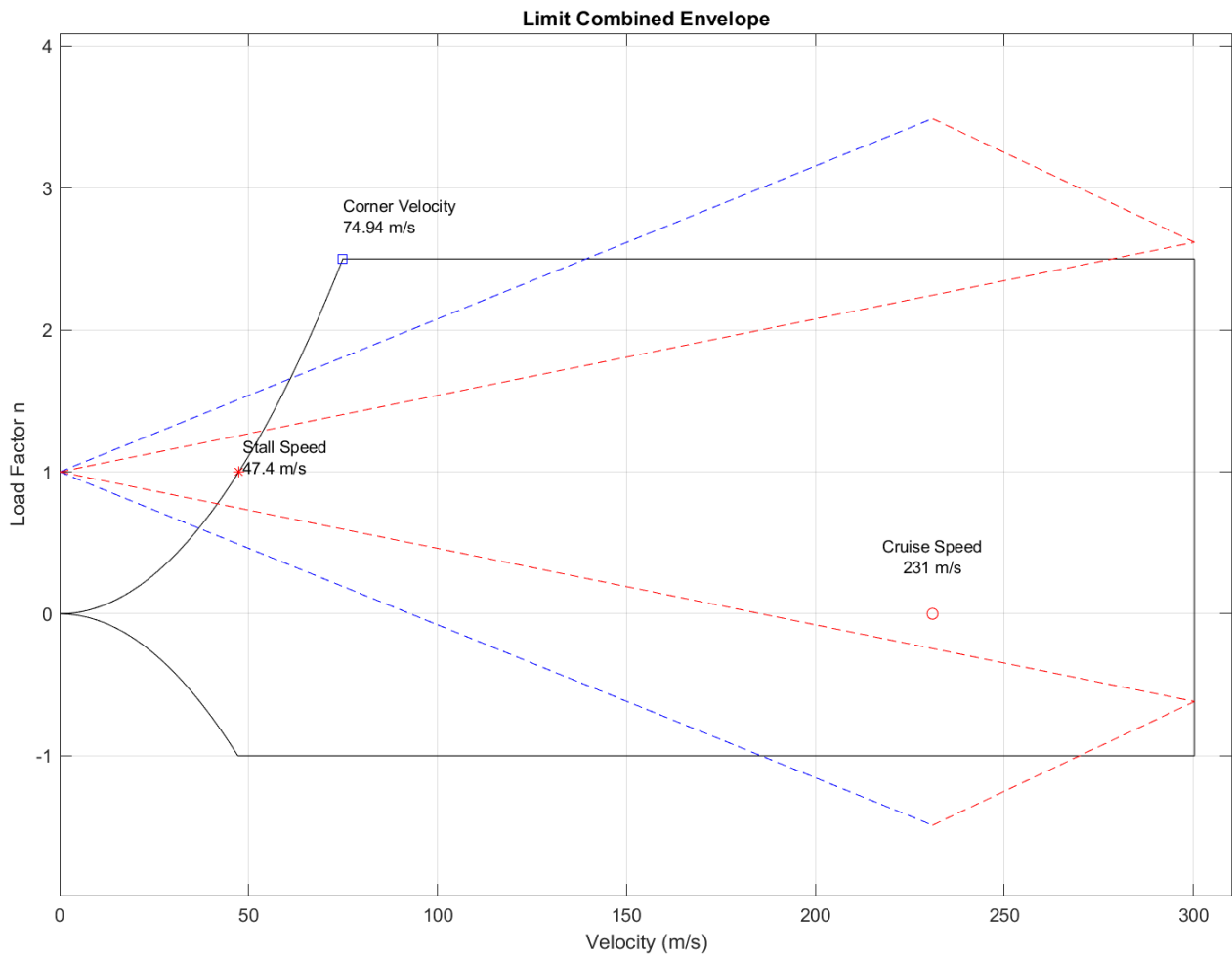**Figure E.1**: Mass breakdown for CHANGE and A220-300

Figure E.2: Payload-Range Diagram

Appendix F Load Envelope

Limit Combined Envelope

Appendix G Technical Drawing

In the following a technical drawing of CHANGE is provided. All lengths are given in metres.

47.15

10.65

3.74

12.9°

5.18

3.91

3.80

9.04

14°

47.15
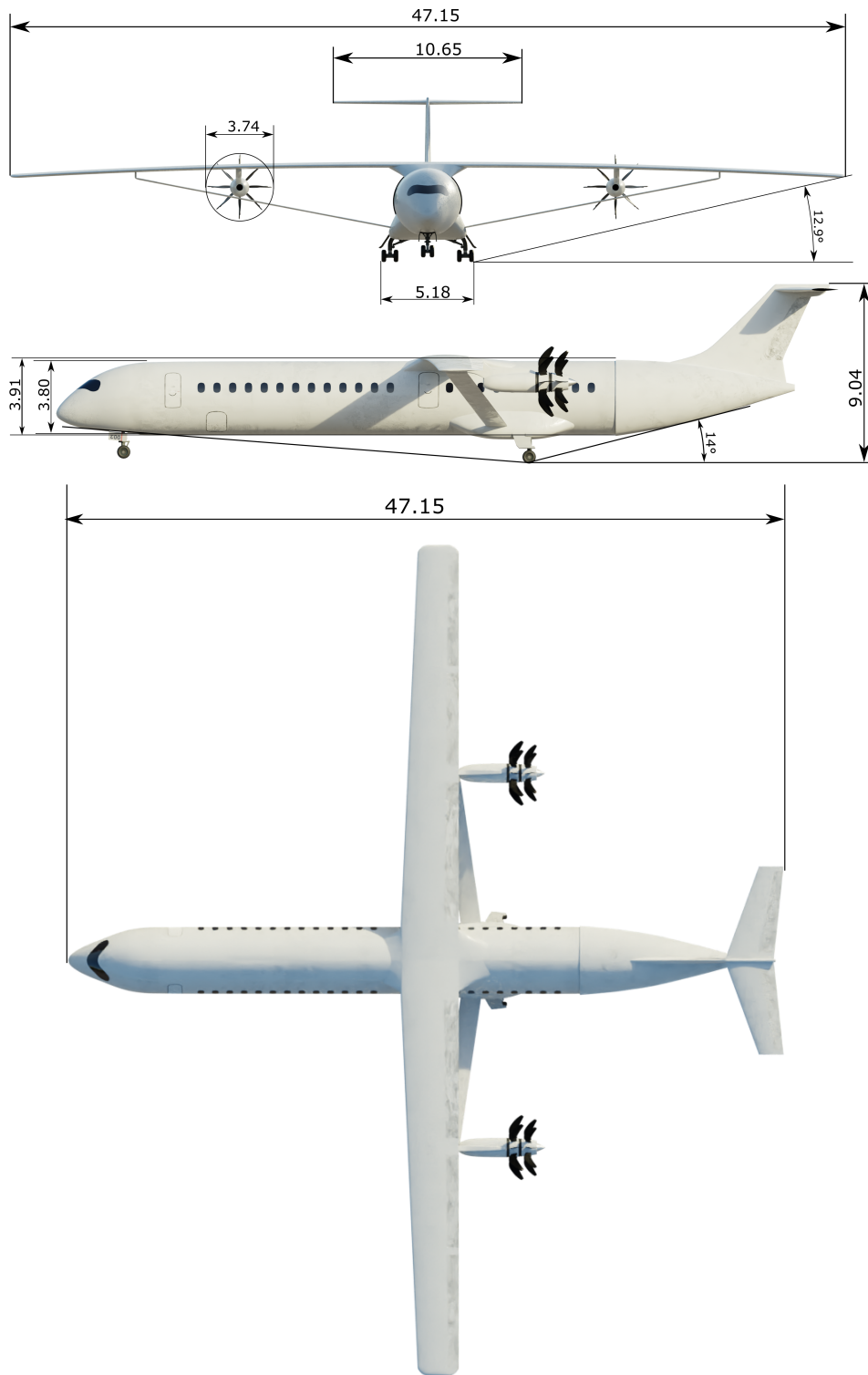
References

[1] IEA. *Aviation*. Paris, 2020. URL: https://www.iea.org/reports/aviation (visited on).

[2] Marcus O. Köhler et al. "Impact of perturbations to nitrogen oxide emissions from global aviation". In: *Journal of Geophysical Research* 113.D11 (2008). ISSN: 0148-0227. DOI: 10.1029/2007JD009140.

[3] Dean Foreman. *Is The World About To See An Oil Shortage?* URL: https://www.api.org/news-policy-and-issues/blog/2021/02/24/is-the-world-about-to-see-an-oil-shortage. (accessed: 18.07.2021).

[4] *Flightpath 2050: Europe's vision for aviation ; maintaining global leadership and serving society's needs ; report of the High-Level Group on Aviation Research*. Policy / European Commission. Luxembourg: Publ. Off. of the Europ. Union, 2011. ISBN: 978-92-79-19724-6.

[5] *Population density dataset*. URL: https://neo.sci.gsfc.nasa.gov/view.php?datasetId=SEDAC_POP. (accessed: 14.07.2021).

[6] *Airbus Global Market Forecast 2019-2038*. 2019. URL: https://gmf.airbus.com/assets/pdf/Airbus_Global_Market_Forecast_2019-2038.pdf?v=1.0.1. (accessed: 14.07.2021).

[7] B. Kaercher. *Formation and radiative forcing of contrail cirrus*. May 2018, p. 1824.

[8] Erwin Moerland et al. "On the Design of a Strut-Braced Wing Configuration in a Collaborative Design Environment". In: *17th AIAA Aviation Technology, Integration, and Operations Conference*. Reston, Virginia: American Institute of Aeronautics and Astronautics, 6052017. ISBN: 978-1-62410-508-1. DOI: 10.2514/6.2017-4397.

[9] Marco Burnazzi. *Design of Efficient High-Lift Configurations with Coanda Flaps*. TU Braunschweig Institut für Strömungsmechanik Germany, 2016.

[10] R. Jensch C.; K.C. Pfingsten; Radespiel. *Design Aspects Of A Gapless High-Lift System With Active Blowing*. In: DLRK 2009, Sept. 2009, p. 8.

[11] R. K.C. Pfingsten; Radespiel. *Numerical Simulation of a Wing with a Gapless High-Lift System Using Circulation Control*. In: 47th AIAA 2009-533, Jan. 2009, p. 26.

[12] R. K.C. Pfingsten; Radespiel. *Experimental And Numerical Investigation Of A Circulation Control Airfoil*. In: 47th AIAA 2009-533, Jan. 2009, p. 26.

[13] Fredrik Svensson. "Potential of reducing the environmental impact of civil subsonic aviation by using liquid hydrogen." PhD thesis. Cranfield: Cranfield University, 2005.

[14] Keith P. Shine. *Radiative Forcing and Climate Change*. Ed. by Encyclopedia of Aerospace Engineering. University of Reading, Reading, UK, 2010. DOI: 10.1002/9780470686652.eae526.

[15] Takuya Hasegawa. *Airbus Symposium: Future perspective on fuel cell technologies*. Ed. by Nissan Research center. 2015. URL: https://sunjet-project.eu/sites/default/files/Nissan-Hasegawa.pdf (visited on 2021).

[16] K. Nikiforow et al. *Power ramp rate capabilities of a 5 kW proton exchange membrane fuel cell system with discrete ejector control*. 2018. DOI: 10.1016/j.jpowsour.2018.01.090.

[17] Department of Energy. *Hydrogen and Fuel Cell Technologies Office Multi-Year Research, Development, and Demonstration Plan*. Ed. by Office of Energy Efficiency & Renewable Energy. Washington DC, 2014. URL: https://www.energy.gov/sites/default/files/2017/05/f34/fcto_myrdd_fuel_cells.pdf (visited on 2021).

[18] Qinghe Li et al. *A Review on Temperature Control of Proton Exchange Membrane Fuel Cells*. 2021. DOI: 10.3390/pr9020235. URL: https://www.mdpi.com/2227-9717/9/2/235/htm (visited on 2021).

[19] W.A.N. W. Mohamed and M. Haziq M. Kamil. *Hydrogen preheating through waste heat recovery of an open-cathode PEM fuel cell leading to power output improvement*. 2016. DOI: 10.1016/j.enconman.2016.07.046.

[20] Romina Ronquillo. *Understanding Heat Exchangers*. Ed. by Thomas Publishing Company. 2021. URL: `https://www.thomasnet.com/articles/process-equipment/understanding-heat-exchangers/` (visited on 2021).

[21] Willy J.G. Bräunling. *Flugzeugtriebwerke*. Berlin, Heidelberg: Springer Berlin Heidelberg, 2015. DOI: `10.1007/978-3-642-34539-5`.

[22] Mark D. Guynn et al. *Performance and Environmental Assessment of an Advanced Aircraft with Open Rotor Propulsion*. Ed. by NASA. Hampton, Virginia, 2012. DOI: `10.13140/RG.2.1.4847.3687`.

[23] I. Thirkell A.; Chen R.; Harrington. *A Fuel Cell System Sizing Tool Based on Current Production Aircraft*. In: SAE International 2017, Sept. 2017, p. 12. DOI: `10.4271/2017-01-2135`.

[24] M. Oehlke. *Masseabschätzung eines Wasserstoff-Außentanks für ein Turboprop-Verkehrsflugzeug*. June 2009, p. 103.

[25] Keith P. Shine. *Radiative Forcing and Climate Change*. Ed. by Encyclopedia of Aerospace Engineering. University of Reading, Reading, UK, 2010. DOI: `10.1002/9780470686652.eae526`.

[26] Frank Anton. *eAircraft: Hybrid-elektrische Antriebe für Luftfahrzeuge*. Potsdam, 2019. URL: `https://www.bbaa.de/fileadmin/user_upload/02-preis/02-02-preistraeger/newsletter-2019/02-2019-09/02_Siemens_Anton.pdf`. (2021).

[27] Emrax d.o.o. (Ed.) *Technical Data and Manual for EMRAX Motors/Generators*. URL: `https://emrax.com/wp-content/uploads/2017/10/user_manual_for_emrax_motors.pdf`. (accessed: 30.06.2018).

[28] Dr. Mykhaylo Filipenko. *Electric and Hybrid-Electric Aircraft: A pragmatic view*. Ed. by Siemens AG. 2019. URL: `https://indico.cern.ch/event/760666/contributions/3481376/attachments/1888359/3113576/20190708_CECICMC_2019_plenary_talk_filipenko_pub.pdf` (visited on 2021).

[29] C. Rohrbach et al. *Evaluation of Wind Tunnel Performance Testings of an Advanced 45 ° Swept Eight-Bladed Propeller at Mach Numbers From 0.45 to 0.85*. Ed. by NASA. 1982. URL: `https://permanent.fdlp.gov/LPS43288/CR-3505.pdf` (visited on 2021).

[30] Rolls-Royce plc, ed. *Trent 1000*. URL: `https://www.rolls-royce.com/products-and-services/civil-aerospace/airlines/trent-1000.aspx#/` (visited on 2021).

[31] Jennifer Kurtz et al. *Fuel Cell Electric Vehicle Durability and Fuel Cell Performance*. Ed. by National Renewable Energy Laboratory. Golden, CO, 2019. URL: `https://www.nrel.gov/docs/fy19osti/73011.pdf` (visited on 2021).

[32] Frank P. Incropera et al. *Fundamentals of heat and mass transfer*. 6. ed. Hoboken, NJ: Wiley, 2007. ISBN: 0-471-45728-0.

[33] *VDI-Wärmeatlas*. Berlin, Heidelberg: Springer Berlin Heidelberg, 2013. DOI: `10.1007/978-3-642-19981-3`.

[34] James G. Coder and Dan M. Somers. "Design of a slotted, natural-laminar-flow airfoil for commercial transport applications". In: *Aerospace Science and Technology* 106 (2020), p. 106217. ISSN: 12709638. DOI: `10.1016/j.ast.2020.106217`.

[35] Fanklin W. Diederich. "A simple approximate method for calculating spanwise lift distributions and aerodynamic influence coefficients". 2013. URL: `https://ntrs.nasa.gov/citations/19930083506`.

[36] Egbert Torenbeek. *Advanced aircraft design: Conceptual design, analysis, and optimization of subsonic civil airplanes*. Aerospace series. Chichester: Wiley, 2013. ISBN: 1118568109. URL: `http://search.ebscohost.com/login.aspx?direct=true&scope=site&db=nlebk&db=nlabk&AN=575163`.

[37] Amir H. Naghshineh-Pour. *Structural Optimization and Design of a Strut-Braced Wing Aircraft*. Virginia Polytechnic Institute and State University, Nov. 1998, p. 116.

[38] Gern; Naghshineh-Pour; Sulaeman; Kapania. *Structural Wing Sizing for Multidisciplinary Design Optimization of a Strut-Braced Wing.* Virginia Polytechnic Institute and State University, Feb. 2001, p. 10.

[39] Hein; Führer; Willberg. *Untersuchungen zur Strukturauslegung im Flugzeugentwurf.* DLR: Institut für Faserverbundleichtbau und Adaptronik Braunschweig, May 2015, p. 115.

[40] L.M. Nicolai. *Fundamentals of aircraft and airship design.* Reston: American Institue of Aeronautics and Astronautics, Inc., 2010.

[41] D. P. Raymer. *Aircraft design: a conceptual approach.* Sylmar: American Institute of Aeronautics and Astronautics, 1989. ISBN: 9780930403515.

[42] *Airplane Design: Part I, Preliminary Sizing of Airplanes.* Ottawa,Kansas: Roskam Aviation and Engineering Corporation, 1985.

[43] J. Thorbeck. *From Aircraft Performance to Aircraft Assessment.* DLR, 2007.

[44] J. Soone. *Briefing - Sustainable aviation fuels.* Nov. 2020.

[45] Buli N.; Abnett K.; Twidale S. *EU carbon price hits record 50 euros per tonne on route to climate target.* 2021. URL: https://www.reuters.com/business/energy/eu-carbon-price-tops-50-euros-first-time-2021-05-04/.

[46] A. Anderson ;A. Karthikeyan ;C. Ramesh Kumar ; S. Ramachandran ;T.R. Praveenkumar. *Lowest emission sustainable aviation biofuels as the potential replacement for the Jet-A fuels.* 2020.

[47] J.I. Hileman; R.W. Stratton;P.E. Donohoo. *Energy Content and Alternative Jet Fuel Viability.* 6. 2010.

[48] A. Bauen;N. Bitossi;L. German;A. Harris;K. Leow. *Sustainable Aviation FuelsStatus, challenges and prospects of drop-in liquid fuels, hydrogen and, electrification in aviation.* 2020.

[49] McKinsey and Company. *Hydrogen-powered aviation A fact-based study of hydrogen technology, economics, and climate impact by 2050.* 2020. URL: https://www.fch.europa.eu/sites/default/files/FCH%5C%20Docs/20200507_Hydrogen%5C%20Powered%5C%20Aviation%5C%20report_FINAL%5C%20web%5C%20%5C%28ID%5C%208706035%5C%29.pdf. (accessed: 14.07.2021).

[50] Christopher K. Droney, N. Harrison, and G. Gatlin. "SUBSONIC ULTRA-GREEN AIRCRAFT RESEARCH : TRANSONIC TRUSS-BRACED WING TECHNICAL MATURATION". In: 2018.

[51] IATA. *Aircraft Technology Roadmap to 2050.* URL: https://www.iata.org/contentassets/8d19e716636a47c184e7221c77563c93/technology20roadmap20to20205020no20foreword.pdf.

[52] Robert J. Englar et al. "Circulation Control Technology Applied to Propulsive High Lift Systems". In: *SAE Transactions* 93 (1984), pp. 296–308. ISSN: 0096736X. URL: http://www.jstor.org/stable/44467145.

[53] A. STUART. "The unducted fan engine". In: *21st Joint Propulsion Conference.* Reston, Virigina: American Institute of Aeronautics and Astronautics, 1985. DOI: 10.2514/6.1985-1190.

[54] Jennifer Harbaugh. "NASA Covers Large SLS Liquid Hydrogen Tank with Foam Insulation". In: *NASA* (2019). URL: https://www.nasa.gov/exploration/systems/sls/multimedia/liquid-hydrogen-tank-covered-with-foam-insulation.html (visited on).

[55] Ramon Beck. *Anfertigung einer Potentialstudie für die Verwendung von Wasserstoff und dessen Speicherung für den domestic market im Flugbetrieb.* Ed. by TU-Berlin. Berlin, 2019.

[56] *A220 Airport planning publication APP.* 2021.